The DOI for this manuscript is doi: 10.1175/MWR-D-16-0075.1

Space-Time Evolution of the Low- and High-Frequency Intraseasonal Modes of the Indian Summer Monsoon

Nirupam Karmakar

Centre for Atmospheric and Oceanic Sciences, Indian Institute of Science, Bangalore, India

Arindam Chakraborty* and Ravi S Nanjundiah.

Centre for Atmospheric and Oceanic Sciences, Indian Institute of Science, Bangalore, India

Divecha Centre for Climate Change, Indian Institute of Science, Bangalore, India.

**Corresponding author address:* Arindam Chakraborty, Centre for Atmospheric and Oceanic Sciences, Indian Institute of Science, Bangalore-560012, India.

E-mail: arch@caos.iisc.ernet.in

ABSTRACT

In this study, rainfall estimates by the Tropical Rainfall Measuring Mission are used to understand the spatiotemporal structures of convection in the intraseasonal timescale and their intensity during the boreal summer over south Asia. A quantitative analysis on how these intraseasonal modes modulate the central Indian rainfall is also provided.

Two dominant modes of variability with periodicities of 10–20-days and 20–60-days are found, with the latter strongly modulated by sea surface temperature. The 20–60-day mode shows northward propagation from the equatorial Indian Ocean linked with eastward propagating modes of convective systems over the tropics. The 10–20-day mode shows a complex space-time structure with a northwestward propagating anomalous pattern emanating from the Indonesian coast. This pattern is found to be interacting with a structure emerging from higher latitudes propagating southeastwards, the development of which is attributed to the vertical shear of the zonal wind. The two modes exhibit profound variability in their intensity on the interannual time scale and they contribute a comparable amount to the daily rainfall variability in a season. The intensity of the 20–60-day and 10–20-day modes show a significantly strong inverse and direct relationship with the all-India June–September rainfall, respectively.

This study establishes that the probability of the occurrence of substantial rainfall over central India increases significantly if the two intraseasonal modes simultaneously exhibit positive anomalies over the region. The results presented in this paper will provide a pathway to understand, using observations and numerical model simulations, intraseasonal variability and its relative contribution to the Indian summer monsoon. It can also be used for model evaluation.

1. Introduction

One of the most widely-studied topics regarding the Indian summer monsoon is its intraseasonal variability (ISV), essentially because of its intense socio-economic impact on the enormous agrarian population of the Indian subcontinent. ISV is often delineated as active-break cycles of precipitation over India with a periodicity of around 30–60-days (Yasunari 1979; Sikka and Gadgil 1980). This linking of periodicity to monsoon ISV implies that certain oscillations are responsible in initiating ISV. These oscillations are called monsoon intraseasonal oscillations (ISOs) (Webster et al. 1998; Annamalai and Slingo 2001; Goswami and Ajaya Mohan 2001; Goswami 2005; Chakraborty and Nanjundiah 2012; Karmakar et al. 2015). ISOs are often connected to the northward propagation of convective cloud bands from the equatorial Indian Ocean (Yasunari 1979; Sikka and Gadgil 1980). Such propagation has a typical latitudinal scale of 30° during a normal monsoon year (Chakraborty and Nanjundiah 2012). This was further confirmed using numerical simulations (Chakraborty and Nanjundiah 2014). It is argued that at least some of these poleward propagations of convection are generated by the eastward moving Madden-Julian oscillations (MJO) (Julian and Madden 1981; Lau and Chan 1986; Singh et al. 1992; Yoo et al. 2010). However, Klingaman et al. (2008) concluded that the future state of the ISO over the Indian region is dependent upon the current state of oscillation over India and not over the equatorial Indian Ocean. These ISOs stem from the dynamical feedback between large-scale circulation and organized convection, and, hence, they are governed by internal dynamics (Goswami 2005, and references therein). This chaotic internal dynamics can crucially limit the predictability of monsoon precipitation from medium- to long-range (Sperber et al. 2001; Rajeevan 2001; Goswami 2005). It has been demonstrated by several studies that ISOs can modulate the interannual variation of rainfall (Hoyos and Webster 2007; Ajaya Mohan and Goswami 2003; Sperber et al. 2000). Also, it has

been shown that the rainfall associated with ISV can strongly affect the Ganges-Brahmaputra river discharge (Jian et al. 2009). Webster and Hoyos (2004) argued that the forecasts of ISV during the monsoon season over India are of more value in agriculture and water resource management than the mean summer rainfall forecasts. Therefore, understanding the spatiotemporal evolution of these ISOs and how these ISOs vary interannually is necessary to improve the predictability of monsoon precipitation on a seasonal and subseasonal scale.

Several studies have been undertaken since the late-1970s towards understanding the spatiotemporal structure of the monsoon ISV and its association with the total rainfall over India (see Goswami 2005; Gadgil 2003; Webster et al. 1998, and references therein). Krishnamurthy and Shukla (2000) suggested that the Indian monsoon rainfall consists of a seasonally persistent mode and a fluctuating intraseasonal component. Later, in another study, they separated out the seasonally persisting component and the two ISO modes with a periodicity of 45- and 20-days in the Indian summer monsoon rainfall (Krishnamurthy and Shukla 2007). They concluded that although ISOs strongly influence the nature of the daily rainfall anomaly, their contribution to the seasonal mean rainfall is negligible. Singh et al. (1992) also concluded that the intensity of the ISO does not exhibit any linear relationship with the seasonal mean rainfall over India or the phases of the El-Niño Southern Oscillation (ENSO). However, Lawrence and Webster (2001), using outgoing longwave radiation (OLR) data, concluded that ISO (25–80-days) intensity is inversely proportional to the total Indian summer monsoon rainfall. A few studies have also shown that dominant ISOs exhibit a longer timescale during the drought years (Yasunari 1980; Rajeevan et al. 2010). Moron et al. (2012) concluded that the monsoon rainfall is mainly dominated by a modulated annual cycle, but ISO (30–60-days) plays an influential role when the annual cycle is neutral during the onset and withdrawal stages of the monsoon. Yoo et al. (2010), using a hidden Markov model, examined the 40–50 day oscillation in pentad rainfall data. They suggested the existence

of the nonlinear influences of ENSO on the ISO. Annamalai and Slingo (2001) showed that about one-fourth and two-thirds of the intraseasonal variability is explained by high and low frequency ISO modes, respectively. Lee et al. (2013) using OLR and low level wind data studied the quasi-oscillations of a period of 30–60-days (northward propagating) and 10–30-days (northwestward propagating). A recent study by Karmakar et al. (2015) investigated the ISO modes of the Indian summer monsoon rainfall (viz., 20–60-days and 10–20-days) and found that during the past six decades the intensity of the low-frequency ISO mode (20–60-days) has decreased significantly.

Since the discovery of intraseasonal variability in the monsoon, most of the studies have been focused on the low-frequency ISO leaving the high-frequency ISO comparatively less explored. An analysis of the various components of the monsoon system was done in Krishnamurti and Bhalme (1976), where they found a dominant biweekly signal from a spectral analysis. The northwestward propagating characteristic of the 10–20 day oscillation was reported first in Murakami (1976). A comprehensive study on the structure of the 10–20 day mode in wind data and how it can affect the Indian monsoon rainfall was done by Chen and Chen (1993). This 10–20-day mode was found to be a westward-moving equatorial Rossby wave having a wavelength of about approximately 6,000 km (Chatterjee and Goswami 2004). Kikuchi and Wang (2009) studied the 10–20-day signals over the entire tropics and concluded that this mode over the Indian monsoon region originates in the tropics and moves westward before dissipating over the subtropics.

Nevertheless, there are certain areas in which we need a better understanding. For example:

1. Low-frequency ISO has been studied extensively in the past few decades, but mainly in terms of either wind or OLR data due to the lack of quality precipitation data over the tropics. Also, since the high-frequency ISO mode has not been studied with the same rigour, one can ask: what are the structures of the ISO modes seen in the rainfall?

2. ISV over the Indian region shows different strengths and characteristics in different years, which means it has a strong interannual variability. So, a statistically significant index to measure the strength of the ISO modes can be useful in understanding the ISV of a particular year.

3. How do the ISO modes modulate the rainfall anomalies over India?

4. Can information about ISO phases lead towards a better understanding of the rainfall over certain regions?

Given the nonlinear and multiscale structure in both time and space of the Indian monsoon rainfall, fulfilling these objectives demands a conscientious analysis of high-quality data over the region. Most of the studies in the past studied monsoon ISV using linear filters (Fourier-based filters) or empirical orthogonal functions (EOFs). But, in principle, linear filtering can hinder the fundamental understanding of a nonlinear, chaotic system like the monsoon. The limitations of EOF analysis are discussed in detail in Monahan et al. (2009). On the other hand, multichannel singular spectrum analysis (MSSA)-like techniques use the temporal structure present in the data while incorporating the EOF technique to understand the dynamical behaviour of the system.

We aim to provide a comprehensive study on the ISO modes seen in the Indian monsoon rainfall and how these modes modulate the rainfall over the central Indian region. We identify the ISO modes in the Indian monsoon rainfall and investigate their behaviour in space and time while calculating the seasonal intensity of these modes using MSSA (Ghil et al. 2002). The next section describes the datasets used in this study. The methodology adapted in this study is discussed in Section 3. A detailed discussion of results is presented in section 4, followed by the conclusions from this study.

2. Datasets

Tropical Rainfall Measuring Mission (TRMM) 3B42 (V7) daily rainfall data for 1998–2014 (Huffman et al. 2007) have been used for this study. The data are regridded into $1^\circ \times 1^\circ$ using bilinear interpolation for computational ease as we are focusing on large-scale intraseasonal features.

We also use the ECMWF ReAnalysis (ERA)-Interim dataset (Dee et al. 2011) and the NOAA (National Oceanic & Atmospheric Administration) OISST (Optimum Interpolation Sea Surface Temperature) version 2 daily data (Reynolds et al. 2007) and interpolated OLR data (Liebmann and Smith 1996) (provided by the NOAA/OAR/ESRL PSD, Boulder, Colorado, USA) for the same period (1998–2014; 1998–2013 for OLR) to understand the features seen in other fields along with rainfall ISOs in the monsoon season.

3. Methodology

The entire analysis has been performed over the south Asian monsoon domain (10°S to 35°N and 60°E to 110°E) unless otherwise specified. We define daily rainfall climatology as the mean on each calendar day over the 17-yr period. On subtracting this climatology from a particular year's daily rainrate, the daily rainfall anomaly is obtained. Very high frequency fluctuations related to synoptic variability were removed by performing a 5-day running mean on this anomaly data. Each year's May–October data (since our aim is to investigate boreal summer monsoon ISOs) are then centered and fed into the multichannel singular spectrum analysis (MSSA) algorithm to extract intraseasonal spatio-temporal modes. An extended monsoon period is taken for an increased number of samples for MSSA; however, subsequent analyses are done using June–September data.

a. Multichannel singular spectrum analysis (MSSA)

The considerable use of MSSA during the last two decades has been seen in many fields of the geosciences (Ghil et al. 2002) including the Indian monsoon (Krishnamurthy and Shukla 2007; Moron et al. 2012; Karmakar et al. 2015), to analyse the spatiotemporal behavior of short and noisy timeseries. Unlike that in a simple harmonic analysis or a fast Fourier transformation, the shape and bandwidth of the filters in MSSA are functions of the input data themselves. This advantage of the MSSA technique is used to understand the unknown or partially known dynamics of a given dynamical system (Broomhead and King 1986). Especially when the given timeseries is short and noisy, MSSA can systematically extract the coherent spatiotemporal signals, and can be more useful than other conventional spectral analyses. Because of its data-adaptive basis functions, this method can detect anharmonic oscillations, originating from nonlinear phenomena. We refer to Plaut and Vautard (1994) or Ghil et al. (2002) for the computational details of MSSA.

We performed a conventional principal component analysis (PCA) to retain 50 PCs (explaining almost 95% of the total variance every year; the results are insensitive to slight changes in the number of PCs retained) and carry the PCs (which are orthogonal by definition) as different channels into MSSA. A lag-covariance matrix is then constructed with lags ranging from 0 to $M-1$, where M is the window length for the daily data (in this study, we used a window length of 60 days). MSSA then diagonalizes this lag-covariance matrix. Following Plaut and Vautard (1994), there may exist an oscillation in the system when two eigenvalues are nearly equal. In such conditions, a phase quadrature exists between the successive space-time EOFs (ST-EOFs) and temporal PCs (ST-PCs). The period of the oscillation is the same as the period of the eigenvectors themselves, and the spatial pattern is similar to one of them. Hence, the ST-EOFs obtained here capture oscillatory behaviour in time through oscillatory pairs, which cannot be seen via the standard PCA.

For noisy data like the monsoon rainfall, MSSA can give a very useful delineation of the nonlinear features in the system.

We have reconstructed the individual components (called reconstructed components or RCs) of the system's behaviour by convolving the corresponding ST-PCs with the ST-EOFs (Vautard et al. 1992; Plaut and Vautard 1994). The original data and the RCs have the same length, and all the RCs add up to the actual input data. These RCs characterize a narrowband of the full frequency spectrum and they separate out the part of the signal associated with an oscillation. In the following discussion, RC(i, j) indicates the sum of RCs associated with eigenmodes i and j.

A statistical test is performed to prevent any random fluctuation, and specifically noise, being treated as an oscillation. The variance captured by an ST-EOF is compared with that present for the same in 1000 red-noise surrogates for this purpose (Allen and Robertson 1996; Ghil et al. 2002). Also, to overcome the artificial variance compression problem, which is seen in most PCA methods, a modified varimax rotation of the ST-EOFs (25 eigenvectors are rotated here) is done (Groth and Ghil 2011). This also improves physical interpretability.

b. Phase composites

To understand the evolution of the oscillation, the first PC of a particular ISO mode is used and the amplitude and phase angle are estimated as in Moron et al. (1998). The phase angle $(\eta(t))$ lies in (0,2π) and for the portrayal of the oscillation, we have divided the phase-plane into eight equal intervals. Then averaging the reconstruction, regardless of the amplitude, over all the occurrences in a particular phase, gives a phase composite.

One of the goals in this work is to measure the variability of rainfall on the low- and high-frequency intraseasonal scale every year. For that purpose, we feed each year's May–October data separately into MSSA. This gives the advantage of using the significant eigenvalues as a measure

of the amplitude of the variability in the aforementioned scales, from which we can define the ISO intensity each year. The method we adopted is applied to a theoretical dataset to demonstrate its capability in extracting the intensities of different oscillatory modes mimicking the ISOs over India, and is presented in the supplementary material.

4. Results

Over the entire south Asian monsoon domain, a substantial spatial variability in the climatological mean and the standard deviation of June-September daily mean rainfall can be seen (Figure 1). Heavy rainfall over the Western Ghats of India, the Myanmar coast, the northern Bay of Bengal (BoB), and the Himalayan foothills is observed. There are regions, especially the head BoB and the Western Ghats, which show high variability on a daily time scale. There exists a spatial homogeneity (uniformity) in the daily climatology, as well as in standard deviation, over the Central Indian (CI) region.

a. Low-frequency ISOs (LF-ISO)

1) EXTRACTION AND STRUCTURE OF LF-ISO MODES

Upon applying MSSA, several significant oscillatory modes with periodicities between 10 to 60 days are detected every year. These modes together represent the broad spectrum of the monsoon ISOs. Taking 1998 as an example, the leading pair of eigenmodes (modes 1 and 2) describes 33-day oscillation (Figure 2). There are two other significant modes with a periodicity of more than 20 days (one of 21 days and the other of 27 days) but they are not characterised by eigen-pairs.

The phase-composite structure of the RC(1,2) for 1998 gives a clear picture of the northward propagation over the south Asian monsoon region along with an eastward movement in the equatorial region (Figure 3a). The eight phases are, essentially, in cyclic order and are separated typically

by 4–5 days. The generation of the large-scale convection over the equatorial Indian Ocean region and its propagation towards the Indian land can be observed in these eight phases. The convective pattern then dissipates over the Himalayan foothills. The northward propagation associated with an eastward movement along the equator, and the tilted structure of anomalous rainfall associated with low-frequency ISO can be seen here. These propagation characteristics are very similar to the low-frequency ISO patterns reported in Krishnamurthy and Shukla (2007) or Lee et al. (2013). Phases 5–8 represent anomalies of the oscillation 180° apart from the phases 1–4. These 8 phases resemble the typical active-break cycle over the Indian region.

The phase-composite structures of the subsequent significant eigenmodes in 1998 with a periodicity of more than 20 days (RC(4) or RC(7)) also show similar dominant characteristics of northward propagation, but with a lower magnitude (not shown). The eigenmodes which have a periodicity of more than 20 days, typically show the patterns described in Figure 3a. Based on this, all the significant pairs (oscillatory modes) with a periodicity of 20-60 days are identified as the northward propagating low-frequency ISO. The extraction and reconstruction of all such modes provide the northward moving low-frequency intraseasonal features. This is done to represent the low-frequency intraseasonal variability, which can be highly anharmonic, by a combination of oscillatory modes, whose dominant spatiotemporal characteristics are similar (northward propagation) and posses a periodicity of 20–60 days. We define this reconstructed part as low-frequency ISO (LF-ISO). For example, during 1998, the LF-ISO will be the sum of RC(1,2), RC(4) and RC(7). We normalise the variance summed up over the LF-ISO scale (obtained from the eigenvalues of the significant eigenmodes) with that year's total variability and define it as the LF-ISO index for each year. This index is presented as a percentage of the total variability in the daily rainfall anomaly (5-days smoothed). The phase composite structure for LF-ISO averaged over all the years shows characteristics similar to the RC(1,2) (northward propagation) for 1998 (Figure

3b). The LF-ISO variability is more intense over the BoB and the eastern equatorial Indian Ocean than over the Indian landmass. However, within the Indian subcontinent, the western parts have the highest LF-ISO variability.

The normalized indices for LF-ISO intensity for every year between 1998 and 2014 are shown in Figure 4a. A large variability in the amplitude of the LF-ISO index is seen. For example, the 2005 June–September rainfall is marked by distinct northward propagating convective bands separated by an intraseasonal timescale (Figure 5a and c). The intraseasonal variability is also evident in the daily accumulated rainfall over CI, which shows distinct peaks associated with these northward-propagating convective bands. This suggests maximum LF-ISO intensity in 2005, whereas in 2011, LF-ISO activity is almost absent (Figure 4 and 5b and d). The non-normalized timeseries of LF-ISO indices shows that the LF-ISO can explain between 17–42% of the total (5-days smoothed) variability in each season (not shown). The northward propagations from the equator are much more prominent in 2005 than in 2011. These propagations along 80°E are clearer in Figures 6a and b for 2005 than for 2011. The existence of a southward propagation from slightly north of the equatorial region can also be seen. The longitude-time diagram at 15°N in Figures 6c and d shows stronger and more prominent eastward propagations of convection from the AS in 2005. It also suggests that LF-ISO modes are stronger in 2005 than in 2011 over both land and ocean. In summary, Figures 5 and 6 suggest strong northward and eastward propagations with about 30 days periodicity in 2005 which is captured in the LF-ISO index timeseries in Figure 4a. But in 2011, the signals are much weaker, especially during the later stage of the monsoon, and are absent over the land.

The LF-ISO intensity is negatively correlated with the CI averaged rainfall anomaly (R=-0.58, significant at the 5% level) and the all-India averaged rainfall anomaly (R=-0.64, significant at the 5% level; rainfall considered over Indian land excluding the hilly regions over the north and

northeast; Tables 1, 2 and Figure 4), which supports the results found in Lawrence and Webster (2001). It is also found that the rainfall anomalies over the BoB, the AS and the central equatorial Indian Ocean (CEIO) are not significantly correlated with the LF-ISO intensity over the south Asian region (Table 1). It is worth noting that a strong LF-ISO intensity can be seen when there exist El-Niño-like situations (Table 2). Based on observing these 17 years, Figure 4 and Table 2 suggest that Indian Ocean dipole (IOD) conditions show very little correlation with the intensity in LF-ISO associated rainfall. Also, looking into the atmospheric component of IOD, viz. the equatorial Indian Ocean oscillation (EQUINOO) defined based on the OLR over EEIO and WEIO (Francis and Gadgil 2013), we found no significant correlation between LF-ISO intensity and EQUINOO (Figure 4 and Table 2).

2) LF-ISO AND THE COMPOSITE STRUCTURES OF SST AND CIRCULATION PATTERNS

We have investigated the behavior of SST and circulation patterns in different phases of LF-ISO to gain an insight into how SST and atmospheric conditions evolve. In Figure 7, the composite structures of SST and positive specific humidity (at 925 hPa level) anomalies for all the 17-years associated with the phases in Figure 3b are shown. In phase 1, the dominant positive SST anomaly pattern is seen over the northern BoB and the AS. However, this SST anomaly is generated over the central and eastern equatorial Indian Ocean in phases 3–4 and moves northward in subsequent phases. An eastward movement of SST along the equator in the low-frequency intraseasonal timescale was documented in Krishnamurti et al. (2007). But we do not observe clear indication of eastward movement over the equatorial Indian Ocean. However, the anomalous SST maximum along the equator shifts eastward in the western Pacific in phases 5–8. Similar to LF-ISO rainfall, SST also shows northward propagation after the positive anomaly gets established the Sumatra coast (phase 4). Interestingly, the SST patterns lead the LF-ISO convective anomalies typically by

2–3 phases (approximately 10–15 days). For example, the LF-ISO associated rainfall is maximum over CI, the BoB and the eastern AS in phase 2, but the SST over the BoB and the AS is warmest in phase 8. This lead-lag relationship is clearer in a phase-latitude diagram over the BoB (Figure 8a). A similar conclusion of this lead-lag relationship was also reported in Klingaman et al. (2008). Two SST maxima (the same as LF-ISO related convection) can be seen over the BoB: one over the equatorial region and the other over the head BoB. These anomalous SST patterns stretch from the western Pacific to the AS in the northwest to the southeast direction. Although the variability in SST anomalies is not large (0.2–0.3 K) in the composites because of averaging across all the years, in specific events these anomalies can rise as high as 1.5 K over particular locations.

Lower tropospheric positive specific humidity anomalies in Figure 7 and LF-ISO related convection are co-located in almost all the phases. Similar to LF-ISO convection, the total column water in the atmosphere also propagates eastward along the equator (not shown) and northward from the deep tropics (Figure 8b). The peaks in atmospheric moisture and convection go almost in phase. The low-level divergence composite estimated based on the eight phases of the LF-ISO phases shows a negative anomaly (convergence) over the CEIO in phase 4 that moves eastward while becoming stronger in subsequent phases (Figure 9). The convergence band shows similar northward propagation as of LF-ISO convection. The northward propagation of low-level convergence at 90°E can be seen in Figure 8c. The maximum convergence slightly leads the LF-ISO convection maximum near the equator. But this lead is not seen in the head BoB region. However, interestingly, there exist patches of divergence within the large-scale northward moving band of convergence in some phases (e.g., 2 and 3) seen in the spatial plot. A similar pattern with opposite signs can be seen in phases 6 and 7. Especially, the Western Ghats and the monsoon trough region show an in-phase relationship in the divergence pattern, whereas peninsular and northeast India are in a similar phase. The wind patterns also follow LF-ISO convection and show a strong

cyclonic vortex over the CI region in phase 3 when the positive LF-ISO anomaly is located over there (not shown).

In essence, prior to the positive anomalous LF-ISO convection bring established over CI in phases 2–3, a strong positive anomalous SST can be seen over the BoB and the AS with a lead of 10–15-days in phases 7–1. Following that, over the peninsula and CI, an anomalous convergence zone emerges and flanks the neighbouring oceans for a few days in phases 2–3 with anomalous positive moisture seen over CI shortly after that. Similar patterns can be seen for negative anomalies also.

b. High-frequency ISOs (HF-ISO)

1) EXTRACTION AND STRUCTURE OF HF-ISO MODES

The existence of a high-frequency intraseasonal mode or biweekly mode in different elements of the monsoon has been documented in Krishnamurti and Bhalme (1976). Typically, these high-frequency modes have a periodicity of 10–20-days with a north-westward movement (Murakami 1976; Chen and Chen 1993). Here, similar to LF-ISO earlier, the significant modes in the eigen-spectrum with a periodicity of 10–20-days are classified as HF-ISO. For example, HF-ISO is defined as the sum of RC(11,12), RC(13) and RC(17) for the year 1998 (Figure 2). In Figure 10, the spatio-temporal characteristics of HF-ISO can be seen, where the phase composite structure averaged over all the years on the HF-ISO scale is represented (similar to that of LF-ISO in Figure 3b). These eight phases are separated by about 2 days. Unlike the LF-ISO phases, HF-ISO shows a lower amplitude and a smaller spatial scale.

In phase 1 of the HF-ISO composite (Figure 10), a positive anomaly is located over the eastern equatorial Indian Ocean. This anomaly actually originates in phase 5 in the western equatorial Indian Ocean which propagates eastward, much like LF-ISO, while gradually gaining amplitude

in phases 6, 7 and 8. In phase 1, this anomaly hits the Indonesian coast and two tilted structures are formed over the east-CEIO: one to the south of the equator in the northeast-southwest direction, and the other to the north of the equator in the northwest-southeast direction (marked by dotted lines in phase 1). In phase 2, the north-of-the-equator tilted structure stretches deep into the southern AS and is amplified while shifting slightly towards the north. Phase 3 shows the northward propagation of the northern band and the weakening of the southern band. In the next three phases, this positive anomalous northern band moves further north while gaining amplitude over the BoB. A close look indicates the presence of two convection maxima in the band: one over the BoB (the star shows one maximum and the line adjoining the star indicates the northwestward movement) and the other over the west coast of India (this maximum gradually develops from the northwest-southeast tilted band over the AS and is marked by a straight line) in almost all the phases from 3–8. While the structure over the BoB shows northwestward propagation, the anomaly over the AS moves northward. Subsequently, the BoB structure weakens while moving northwestward and the other maximum amplifies in phase 8. A similar structure is seen with negative anomalies also as phases 5–8 are 180° apart from phases 1–4. HF-ISO does not show a strong variability over the equatorial oceanic region as can be seen for LF-ISO; instead the maximum variability is observed over the BoB region.

Note that the intensity of the positive anomaly over the head Bay and Bangladesh in phases 2 and 3 strengthens after the presence of the dying positive anomaly in phase 1 over that region. This strengthening can be seen for the negative anomaly also in phases 6 and 7. This revival could be related to mid-latitude interactions as we will see in the next subsection. As shown in Figure 11, a positive anomaly pattern generates to the north of 20°N and gradually propagates southeastward while intensifying (marked as a spiral starting from phase 8; the size of the spiral indicates the intensity). This pattern interacts with the northeastward-moving positive anomaly in phases 8–1

and gradually moves eastward while intensifying till phase 3 and then dies off. This is evident in Figure 11a, where southward propagation to the north of 20°N is seen. Northward propagation is visible to the south of 20°N. In the phase-latitude composite diagram in Figure 11b, this is depicted in an average sense. This shows that the southeastward-moving negative anomaly interacts with the northward-propagating negative anomaly in phases 4 and 5.

Unlike LF-ISO, the HF-ISO mode usually shows a greater amplitude for 1–2 months in most of the years during June–September; otherwise it remains less intense. HF-ISO shows maximum variability during July and very low intensity in September over the CI region (not shown). For example, in 2007, the space-time structures of such modes show the maximum intensity during June–July and subside after that even when the seasonal HF-ISO intensity is strongest in that year (Figure 11a). The HF-ISO related northwestward-moving convective bands are prominent over Indian land, especially during the years with strong HF-ISO variability (in Figure 4). To understand this northwestward movement, a curvilinear-phase diagram is shown from the Indonesian coast to CI (Figure 11c). The convection in the HF-ISO band more or less follows the path shown in the map (with black crosses). The convection is initiated over the Sumatra region, and then propagates westward towards the south BoB. It is then amplified before entering the central BoB. Finally, the convection band moves northwestward to Indian land. As the centre moves far inland, the intensity lessens and it dies off over the northwestern part of India.

The normalized HF-ISO index from 1998–2014 is given in Figure 4a. However, the interannual standard deviation of the HF-ISO intensity is smaller than the LF-ISO indices (can be seen in a non-normalized timeseries). The HF-ISO explains about 8–20% of the variability of the daily rainfall anomaly (5-days smoothed) (not shown). An important aspect is that the HF-ISO intensity is significantly positively correlated with the all-India monsoon rainfall (R=0.73; 5% significance level) (Table 2). However, similar to LF-ISO, the HF-ISO index, also, is not correlated to the rain-

fall anomalies over adjacent oceanic regions but significantly correlated to the CI rainfall (R=0.56; 5% significance level) (Table 1). The HF-ISO index is well-correlated with the ENSO and IOD conditions (Table 2). Warmer SST over the eastern Pacific can occur with weaker HF-ISO, whereas colder SST is associated with stronger HF-ISO intensity. HF-ISO intensity usually peaks when there exists a La-Niña-like condition and a positive-IOD-like situation (for example, during 2007). Compared to IOD, its atmospheric component or EQUINOO plays a less important role in modulating HF-ISO intensity (R(IOD, HF-ISO)=0.59; significant at the 5% level, but R(EQUINOO, HF-ISO)=0.33; not significant at the 5% level).

2) HF-ISO AND THE COMPOSITE STRUCTURES OF CIRCULATION PATTERNS

The SST and the specific humidity anomalies depicted in different phases of the HF-ISO composite structure (not shown) indicate that the correspondence between the HF-ISO anomalies and large scale SST anomalies is either absent or is very weak compared to LF-ISO. Also, air-sea coupling may not be as vital as in LF-ISO in the generation of a high-frequency ISV of rainfall over the south and east Asian monsoon region. Specific humidity follows the rainfall patterns associated with HF-ISO, albeit with the magnitude much lower than in the LF-ISO.

It is evident from Figure 12 that over the central Asian region an upper-tropospheric anomalous high appears in phase 8 through 3 (discussed anomalies are significant at 10% level, but not shown in the figure for better visualization). This anomalous high is linked to the upper-level Eurasian wave train emanating from the far west of the Eurasian continent. Because of this, the upper tropospheric easterly wind gets amplified, and this produces a strong vertical shear over northern India in respective phases. As a result, the equatorial Rossby wave instability increases, which, in turn, increases the precipitation over the northern Indian region (Ding and Wang 2007). It can be seen here that prior to the peak in the HF-ISO associated rainfall anomaly over the northern

Indian region (phases 1, 2 and 3 in Figure 10), the central Asian anomalous high develops leading to the enhancement of the easterly vertical shear to the south of it (phases 8 to 2). As evident from Figures 10 and 12, the positive anomaly in HF-ISO precipitation over northern India, and subsequently, over Bangladesh and the northern BoB region amplifies after the increase of the 200 hPa geopotential height over central Asia and the upper tropospheric easterlies south of it. Thereafter, this convection reinforces the upper-tropospheric wave train by exiting a Rossby wave train (Ding and Wang 2007).

In phases 3 and 4 in Figure 12, an upper-tropospheric northerly flow over central Asia and the northern part of India can be seen, which is generated because of the upper-level divergence and strong updraft over the northern Indian region. This northerly flow can be an outcome of enhanced easterlies (Hoskins and Wang 2006). Further, the central Asian anomalous high retreats westward following convection over the region. This occurs because of the Rossby wave response to the heating due to HF-ISO associated precipitation (Gill 1980). Another facet to note is that there exists a positive anomaly in specific humidity, most prominent over the northern AS, and the Persian Gulf in phases 3–5 to the west of the anomalous high at a 200 hPa geopotential height (not shown). The divergence pattern does not show a great association with HF-ISO convection on a large scale, but convergence over the BoB and CI region along with the convection anomaly can be seen (not shown). This mid-latitude interaction in LF-ISO composites is not as clear as it is in HF-ISO (not shown), implying that while the role of SST is quite important in modulating the LF-ISO mode, the HF-ISO mode is governed by various other factors and is influenced by an upper level jet stream.

c. Relationship between the central Indian rainfall and ISO modes

Understanding the relationship between ISO modes and the rainfall over CI can help in understanding predictability, especially at shorter scales. In this section, we aim to provide a comprehensive analysis on the relationship between CI rainfall and ISO modes. We have taken June–September CI (18°–26°N and 75°–82°E; see Figure 1) averaged rainfall (seasonal rainfall over CI is well-correlated with all-India averaged rainfall (R=0.75; significant at 5% level)) and examined how this rainfall is modulated by the phases of LF- and HF-ISO. We have calculated the days when the CI rainfall anomaly is more than a +1 standard deviation and designated as a $+1$-event. Then we have estimated the numbers of those events in the different LF-ISO and HF-ISO phases obtained in Figures 3b and 10 (taking only June–September data for all the years). A similar analysis is done when the CI rainfall is less than -1 standard deviation (-1-event). The result is shown in Figure 13. There are 310 $+1$-events and 281 -1-events in total during these 17 years, out of which almost 60% (in both cases) occurred in LF-ISO phases 2–4 and 5–7, respectively. This is indicated by the horizontal patches of higher probability across phases 2–4 and 5–7 in Figures 13a and b, respectively. However, the distribution of the events in HF-ISO phases does not show such distinctive features as in LF-ISO. Which indicates that the rainfall over the CI region is more influenced by LF-ISO modes than by HF-ISO modes, although it can be seen that HF-ISO further modulates the $+1$-events as its probability of occurrence is less in phase 5 of HF-ISO even when LF-ISO is favourable to produce more rainfall over CI. Phase 5 of HF-ISO represents the state when there exists a negative precipitation anomaly over the CI region. The modulation of -1-events by HF-ISO phases is even stronger when compared the $+1$-events. For example, in phase 7 of LF-ISO, there is generally a high chance of getting a -1-event over CI. But, if HF-ISO is in phase 7 (positive anomaly over CI) then this chance is reduced drastically. In summary, al-

though LF-ISO primarily modulates the rainfall events over CI, HF-ISO plays a significant role in modulating the probability of occurrence of active and break conditions.

To gain a further insight into how the CI rainfall is regulated by the intraseasonal modes, the rainfall averaged over the CI region during 2003 June–October is shown in Figure 14b. The reason we choose 2003 is that in this year LF-ISO and HF-ISO indices show almost equal values (Figure 4). In Figures 14a and c, the LF-ISO and HF-ISO averaged over the same region are shown. There are several troughs and ridges in the time-series indicating the active and break spells over the region. It is clear that in this year, HF-ISO is of comparable magnitude with LF-ISO over CI during late-July to mid-August. LF-ISO is most prominent and shows the maximum amplitude in mid-July and September. It is observed here that during the end of July 2003 the decrease of rainfall over CI is accompanied by both negative LF-ISO and HF-ISO anomalies. However, the rainfall peaks during late–July to late–August (marked by a circle) are not explained by LF-ISO. Observing the HF-ISO time-series, is becomes quite clear that these distinct peaks in the rainfall during this period are associated with high-frequency variability with the LF-ISO mode basically being suppressed till late-August. Examining the peaks of the 2003 June–October rainfall data over CI, we infer that both the ISO modes contribute to monsoon rainfall and active and break conditions are essentially synchronized with both the ISO timescales.

It has been suggested by Krishnamurti et al. (1985) that the break conditions over the monsoon zone can be "an interesting phase locking phenomenon" when the ridges of high pressure associated with low- and high-frequency ISOs appear concurrently over the region. In Figure 15, we show how the mean CI rainfall is modulated by ISO modes as well as the phase-locking between LF- and HF-ISO. The LF-ISO phases are placed in the $x-axis$ as they evolve, and the probability of the occurrence of HF-ISO phases in each LF-ISO phase is estimated. It is inherent that LF-ISO has almost twice the periodicity of HF-ISO–depicted by the fact that LF-ISO phase 1 as well

as phase 5 are favourable for HF-ISO phases 5 and 6. This implies that HF-ISO can well be in phase or completely out of phase with LF-ISO at times. The June–September rainfall over CI is 7.7 mm/day. The CI mean rainfall is 7.9 mm/day if LF-ISO is in phase 1. However, when this is accompanied by HF-ISO phase 5 or 6 (negative anomaly over CI), the mean rainfall decreases to 7 mm/day. On the other hand, in phase 5 of LF-ISO, when the associated positive anomalies are subsiding over the foothills of the Himalayas and a new convection is being formed over the western equatorial Indian Ocean, the mean CI rainfall is 6.9 mm/day. But this mean reduces significantly to 5.2 mm/day when LF-ISO phase 5 is accompanied by HF-ISO phase 5 or 6. So, in LF-ISO phase 1, the LF-ISO and the preferred HF-ISO phases work in an out-of-phase format, whereas, in LF-ISO phase 5, they are in phase to reduce the rainfall over CI. The combined effect of both the ISOs are pronounced when the LF-ISO is in either phase 1 or 5.

Lastly, we use a similar technique to that in Karmakar et al. (2015) to define the active/break episodes of LF- and HF-ISO over the CI region using the area-averaged CI LF- and HF-ISO rainfall timeseries every year (16a and b; see the supplementary material for details). Here, since 1998 was a normal monsoon year over India, we have demonstrated this year as an example. The active, break and transition episodes are derived for both the LF- and HF-ISO modes, and we calculate the percentage of the $+1$ and -1-events occurring in these ISO episodes, respectively, for all the years under consideration (1998–2014). The results are presented in Figures 16c and d as venn-diagrams. This shows that in more than half (56.8%) the times when CI experiences a high rain situation, LF-ISO is in an active episode. Similarly, when there exists a LF-ISO break episode over CI, there is a good chance (57.7%) of less rainfall over the region. However, a substantial number of $+1$- or -1-events occur in the HF-ISO active or break episodes (42.8% and 40.6%, respectively). Occasions on which LF-ISO and HF-ISO are both in active episodes account for 23.4% of the $+1$-events. Almost similar percentage of -1-events occur if they are

both in break episodes. These values are the highest among the intersections of all the LF-ISO and HF-ISO episodes. There are instances when either LF-ISO or HF-ISO is in an active episode and CI experiences a -1-event. Also, when either LF-ISO or HF-ISO is in a break episode some $+1$-events occurred over CI. These instances are reduced markedly if both ISOs are in the same episode. This, again, in a different perspective, indicates that CI rainfall is highly modulated by the characteristics of the ISOs and the stages they are in.

5. Summary and Discussions

It has been known for quite a long time that two intraseasonal modes (low- and high-frequency modes) heavily modulate the Indian monsoon rainfall. Although low-frequency modes were studied extensively in the past few decades, high-frequency intraseasonal modes, especially their space-time characteristics seen in rainfall data and their roles in producing active-break conditions over the Indian region have not been studied very rigorously. In this study, we use MSSA to extract significant components of these two spatio-temporal modes in TRMM daily precipitation data, and present the rich structures over the south Asian monsoon region. We further investigate how the CI rainfall is associated with ISO modes. The major findings made in this study are summarized and discussed as follows.

1. Two dominant modes in ISV in the Indian monsoon rainfall are found: northward propagating low-frequency modes associated with an eastward propagating signal (LF-ISO; 20–60-days periodic) and very complex structured high-frequency modes (HF-ISO; 10–20-days periodic). The low-frequency mode is associated with a tilted structure in the northwest-southeast direction, which propagates northward from the equatorial Indian Ocean to the foothills of the Himalayas. The spatiotemporal pattern seen in this mode matches with the findings in many previous studies using different variables (e.g., Lee et al. (2013)). However, compared to Lee

et al. (2013), we found that LF-ISO associated rainfall anomalies show more variability over the western coast of India and the eastern AS (of amplitude similar to that over the BoB).

2. The intensities of the LF-ISO and HF-ISO modes have a large interannual variability. The LF-ISO and HF-ISO can contribute a substantial amount (ranging between 17%–42% and 8%–20%, respectively, in different years) to the total explained variance of the daily rainfall anomaly (5-days smoothed). LF-ISO usually remains active throughout the monsoon season, but HF-ISO usually shows variability with a comparable magnitude for 1–2 months only during the monsoon months (especially during July). The high negative correlation (R=0.61; 5% significance level) between the LF-ISO and HF-ISO indices can lead to a belief that it comes from the decomposition itself, where orthonormal components (LF-ISO and HF-ISO) contribute to the total variability. But since they add up to just the half of the total variability, the methodology is not solely responsible for this negative correlation. Karmakar et al. (2015) showed that there was a reduction in LF-ISO intensity with an increase in synoptic variability in the last six decades over Indian land. The HF-ISO intensity showed no trend. So, the negative correlation between LF-ISO and HF-ISO intensities are not merely from the methodology itself. Instead, we believe that the underlying dynamics must be playing a major role here. We keep this issue as our future plan. The interannual variability of the LF-ISO and HF-ISO indices are significantly inversely and directly correlated with the all-India averaged rainfall anomaly, respectively. But they are not correlated with the rainfall over the adjacent oceanic regions (Table 1). It is also suggested at this point that when El-Niño-like situations exist, strong LF-ISO modes are observed and La-Niña- and positive IOD-like situations co-occur with strong HF-ISO modes over the Indian region (Table 2). These findings match with the results presented in Lawrence and Webster (2001), except for the LF-ISO-ENSO corre-

lation. This may arise because of differences in the period of the study. However, this study counters the results in Singh et al. (1992), where they have suggested that the intensity of ISO remains the same during drought or flood years. Krishnamurthy and Shukla (2000, 2007) also suggested that, although the ISO modes do not contribute to the seasonal mean rainfall, they can strongly modulate the daily rainfall anomalies in active and break phases. We found that low-frequency ISV exhibits a stronger character (larger spatio-temporal amplitude) in the years when the total rainfall over India is low. The differences in the results may arise possibly because of the difference in the region as well as the period of the study.

3. In the intraseasonal scale, the LF-ISO is strongly associated with the SST over the Indian Ocean and the western Pacific with SST leading LF-ISO rainfall anomalies by 10–15-days. The convergence patterns also show a strong northward movement along with the rainfall LF-ISO modes with a slight lead near the equator, and the moisture anomalies propagate almost in tandem with the rainfall anomalies. Essentially, this goes with the facts presented in Kemball-Cook and Wang (2001) regarding the northward propagation of convection. They suggested that over the Indian monsoon region, the background easterly vertical shear (which is a basic characteristic during the monsoon season) aids the large-scale diabatic heating induced circulation. As a result, a cyclonic vorticity is generated in the northern side of the convection, which boosts lower tropospheric moisture convergence with SST playing a pivotal role. We found that the SST-rainfall relationship is not present in the HF-ISO scale implying that the SST may not be a key driver for the modes in this timescale. This implies that the air-sea coupling plays a key-role in driving the LF-ISO modes, while HF-ISO is governed by several other factors.

4. HF-ISO shows a distinct northwestward propagation over the BoB region the Indian land which can be associated with the equatorial Rossby wave. We also observe a northward propagating branch over the Western Ghats. These patterns match with the results found in Kikuchi and Wang (2009). Although these structures match with the northwestward propagating mode reported in Lee et al. (2013), the HF-ISO mode composite we find differs from them in some aspects. The anomaly structures we found are smaller in scale and exhibit very complex patterns. One possible explanation can be the inclusion of a 30-day mode in their northwestward propagating mode. Also, the regions used in the studies are different and the northwestward propagating mode in OLR/low-level wind can show different characteristics than in rainfall. However, more importantly, we found an anomaly pattern that developed further northwest over India propagates mainly southeastward. The upper tropospheric wind and geopotential height anomalies shed some light on this southeastward propagation at 30°N at the HF-ISO time scale. Basically, a strong easterly vertical shear generated by the anomalous high over central Asia leads to enhanced precipitation (Ding and Wang 2007). The northwestward moving mode interacts with the southeastward moving mode and the anomalies over the head BoB region revive, causing precipitation. But the actual mechanism and scale selection (10–20-days) are yet to be understood.

5. The different periodicities of LF-ISO and HF-ISO leads to the fact that they can be in phase or out-of-phase at times; basically, they can have any phase relationship. However, it is understandable from Figure 15, that particular HF-ISO phases (for example, 5 and 6) prefer to occur in particular LF-ISO phases (1 or 5). This preferential occurrences of the phases of one ISO mode in the other indicate a possible phase-locking between the two ISO modes. Which shows that, although by definition they are independent of each other, there exists

some relationship between them. The physical mechanism behind the interaction of these two modes requires further study. The CI rainfall is highly modulated by the phases of the LF- or HF-ISO modes. HF-ISO can counter the effect of LF-ISO to produce less than average rainfall over the region (for example, phase 1 of LF-ISO in Figure 15). The probability of getting a large number of +1 rainfall events is maximum when both LF-ISO and HF-ISO positive anomalies are present over the CI region. Similarly, break events over CI are caused by the simultaneous arrival of the troughs of LF-ISO and HF-ISO.

In summary, we have presented the structures associated with low- and high-frequency ISV in rainfall. Our study also shows how the existence of a southeastward propagating mode at a 10–20-day timescale towards east-central India from the higher latitudes affects the canonical quasi-biweekly mode structure (north-westward propagation). A possible mechanism is also explained using vertical wind shear. We rely on a data-adaptive technique, MSSA, for the extraction of the ISO modes mainly because of two reasons. First, we intended to measure the intensity of the ISV every year separately and quantify it. Since MSSA is successful in recovering the "skeleton" of the attractor of the system from a short noisy dataset (Ghil et al. 2002), with the eigenvalues giving the estimate of the variance of the modes, we can use the significant eigenvalues to create the index of ISOs as well as observe the dominant space-time patterns. Secondly, compared to other spectral and EOF techniques (e.g., complex PCA), MSSA can self-consistently separate out spatially similar oscillations with different frequency ranges (e.g., see Jiang et al. 1995, and references therein).

The quantitative measure of the modulation of rainfall over CI by the ISO modes found in the study leads to the fact that a rudimentary forecast of the rainfall of about 10–20-days over the region can be made using the knowledge of the ISO phases. Irrespective of the fact that the inter-

annual fluctuations of ISO activity (LF-ISO or HF-ISO) modulate interannual variability during the monsoon or vice versa, the relatively strong association between the two phenomena found in this study is of paramount importance in forecasting monsoon rainfall at different timescales. It is necessary for a dynamical model to represent the ISO modes accurately to perform effectively in predicting total ISMR, particularly in weak monsoons when LF-ISO modes are strong. To this end, the methodologies adopted here provide a framework which can be used for model evaluation.

Finally, synoptic-scale features explain a large portion (almost one-third) of the daily rainfall anomaly within a season over the Indian region (Karmakar et al. 2015). This can restrict the regional-scale predictability on a longer time scale. The relationship between ISO modes and synoptic-scale phenomena over the south Asian domain remains to be analysed, since this can improve the predictability in a short- to medium-range. MSSA-like techniques may be used to advance the predictive skill of the intraseasonal features studied here that capture the substantial variability of the rainfall.

Acknowledgments. The authors are thankful to INCOIS, MoES/CTCZ, and National Monsoon Mission, Government of India, for their support. We thank three anonymous reviewers for their valuable comments that helped to improve our manuscript. We also thank Prof. N. V. Joshi (CES, IISc) for helpful discussions.

References

Ajaya Mohan, R., and B. N. Goswami, 2003: Potential predictability of the Asian summer monsoon on monthly and seasonal time scales. *Meteor. Atmos. Phys.*, **84 (1-2)**, 83–100, doi: 10.1007/s00703-002-0576-4.

Allen, M., and A. Robertson, 1996: Distinguishing modulated oscillations from coloured noise in multivariate datasets. *Climate Dyn.*, **12 (11)**, 775–784, doi:10.1007/s003820050142.

Annamalai, H., and J. M. Slingo, 2001: Active/break cycles: diagnosis of the intraseasonal variability of the Asian summer monsoon. *Climate Dyn.*, **18 (1-2)**, 85–102, doi:10.1007/s003820100161.

Broomhead, D. S., and G. P. King, 1986: Extracting qualitative dynamics from experimental data. *Phys. D*, **20 (2)**, 217–236, doi:10.1016/0167-2789(86)90031-X.

Chakraborty, A., and R. S. Nanjundiah, 2012: Space–time scales of northward propagation of convection during boreal summer. *Mon. Wea. Rev.*, **140 (12)**, 3857–3866, doi:10.1175/MWR-D-12-00088.1.

Chakraborty, A., and R. S. Nanjundiah, 2014: Role of orography in modulating space–time scales of convection over South Asia. *Theor. Appl. Climatol.*, **116 (3-4)**, 549–564, doi:10.1007/s00704-013-0963-4.

Chatterjee, P., and B. N. Goswami, 2004: Structure, genesis and scale selection of the tropical quasi-biweekly mode. *Quart. J. Roy. Meteor. Soc.*, **130 (599)**, 1171–1194, doi:10.1256/qj.03.133.

Chen, T.-C., and J.-M. Chen, 1993: The 10-20-day mode of the 1979 Indian monsoon: Its relation with the time variation of monsoon rainfall. *Mon. Wea. Rev.*, **121 (9)**, 2465–2482, doi:10.1175/1520-0493(1993)121⟨2465:TDMOTI⟩2.0.CO;2.

Dee, D. P., and Coauthors, 2011: The ERA-Interim reanalysis: configuration and performance of the data assimilation system. *Quart. J. Roy. Meteor. Soc.*, **137 (656)**, 553–597, doi:10.1002/qj.828.

652 Ding, Q., and B. Wang, 2007: Intraseasonal teleconnection between the summer Eurasian wave
653 train and the Indian Monsoon. *J. Climate*, **20 (15)**, 3751–3767, doi:10.1175/JCLI4221.1.

654 Francis, P. A., and S. Gadgil, 2013: A note on new indices for the equatorial Indian Ocean oscil-
655 lation. *J. Earth Syst. Sci.*, **122 (4)**, 1005–1011.

656 Gadgil, S., 2003: The Indian monsoon and its variability. *Annu. Rev. Earth Planet. Sci.*, **31 (1)**,
657 429–467, doi:10.1146/annurev.earth.31.100901.141251.

658 Ghil, M., and Coauthors, 2002: Advanced spectral methods for climatic time series. *Rev. Geophys.*,
659 **40 (1)**, 3–1–3–41, doi:10.1029/2000RG000092, 1003.

660 Gill, A. E., 1980: Some simple solutions for heat-induced tropical circulation. *Quart. J. Roy.*
661 *Meteor. Soc.*, **106 (449)**, 447–462, doi:10.1002/qj.49710644905.

662 Goswami, B. N., 2005: South asian monsoon. *Intraseasonal Variability in the Atmosphere-Ocean*
663 *Climate System*, K. M. Lau, and D. E. Waliser, Eds., Springer Praxis, 19–61.

664 Goswami, B. N., and R. Ajaya Mohan, 2001: Intraseasonal oscillations and interannual variability
665 of the Indian summer monsoon. *J. Climate*, **14 (6)**, 1180–1198, doi:10.1175/1520-0442(2001)
666 014⟨1180:IOAIVO⟩2.0.CO;2.

667 Groth, A., and M. Ghil, 2011: Multivariate singular spectrum analysis and the road to phase
668 synchronization. *Phys. Rev. E*, **84**, 036 206, doi:10.1103/PhysRevE.84.036206.

669 Hoskins, B., and B. Wang, 2006: Large-scale atmospheric dynamics. *The Asian Monsoon*,
670 Springer, 357–415.

671 Hoyos, C. D., and P. J. Webster, 2007: The role of intraseasonal variability in the nature of Asian
672 monsoon precipitation. *J. Climate*, **20 (17)**, 4402–4424, doi:10.1175/JCLI4252.1.

673 Huffman, G. J., and Coauthors, 2007: The TRMM multisatellite precipitation analysis (TMPA):
674 Quasi-global, multiyear, combined-sensor precipitation estimates at fine scales. *J. Hydrometeo-*
675 *rol.*, **8 (1)**, 38–55, doi:10.1175/JHM560.1.

676 Jian, J., P. J. Webster, and C. D. Hoyos, 2009: Large-scale controls on Ganges and Brahmaputra
677 river discharge on intraseasonal and seasonal time-scales. *Quart. J. Roy. Meteor. Soc.*, **135 (639)**,
678 353–370.

679 Jiang, N., J. D. Neelin, and M. Ghil, 1995: Quasi-quadrennial and quasi-biennial variability in the
680 equatorial Pacific. *Climate Dyn.*, **12 (2)**, 101–112.

681 Julian, P., and R. Madden, 1981: Comments on a paper by T. Yasunari: A quasistationary appear-
682 ance of 30-to 40-day period in the cloudiness fluctuations during the summer monsoon over
683 India. *J. Meteor. Soc. Japan*, **59**, 435–437.

684 Karmakar, N., A. Chakraborty, and R. S. Nanjundiah, 2015: Decreasing intensity of monsoon
685 low-frequency intraseasonal variability over India. *Environ. Res. Lett.*, **10 (5)**, 054 018, doi:
686 10.1088/1748-9326/10/5/054018.

687 Kemball-Cook, S., and B. Wang, 2001: Equatorial waves and air-sea interaction in the boreal sum-
688 mer intraseasonal oscillation. *J. Climate*, **14 (13)**, 2923–2942, doi:10.1175/1520-0442(2001)
689 014.

690 Kikuchi, K., and B. Wang, 2009: Global perspective of the quasi-biweekly oscillation. *J. Climate*,
691 **22 (6)**, 1340–1359.

692 Klingaman, N. P., H. Weller, J. M. Slingo, and P. M. Inness, 2008: The intraseasonal variability
693 of the Indian summer monsoon using TMI sea surface temperatures and ECMWF reanalysis. *J.*
694 *Climate*, **21 (11)**, 2519–2539.

Krishnamurthy, V., and J. Shukla, 2000: Intraseasonal and interannual variability of rainfall over India. *J. Climate*, **13 (24)**, 4366–4377.

Krishnamurthy, V., and J. Shukla, 2007: Intraseasonal and seasonally persisting patterns of Indian monsoon rainfall. *J. Climate*, **20 (1)**, 3–20, doi:10.1175/JCLI3981.1.

Krishnamurti, T. N., and H. Bhalme, 1976: Oscillations of a monsoon system. Part I. Observational aspects. *J. Atmos. Sci.*, **33 (10)**, 1937–1954, doi:10.1175/1520-0469(1976)033⟨1937:OOAMSP⟩2.0.CO;2.

Krishnamurti, T. N., A. Chakraborty, R. Krishnamurti, W. K. Dewar, and C. A. Clayson, 2007: Passage of intraseasonal waves in the subsurface oceans. *Geophys. Res. Lett.*, **34 (14)**, L14 712, doi:10.1029/2007GL030496.

Krishnamurti, T. N., P. Jayakumar, J. Sheng, N. Surgi, and A. Kumar, 1985: Divergent circulations on the 30 to 50 day time scale. *J. Atmos. Sci.*, **42 (4)**, 364–375, doi:10.1175/1520-0469(1985)042⟨0364:DCOTTD⟩2.0.CO;2.

Lau, K.-M., and P. Chan, 1986: Aspects of the 40-50 day oscillation during the northern summer as inferred from outgoing longwave radiation. *Mon. Wea. Rev.*, **114 (7)**, 1354–1367, doi:10.1175/1520-0493(1986)114⟨1354:AOTDOD⟩2.0.CO;2.

Lawrence, D. M., and P. J. Webster, 2001: Interannual variations of the intraseasonal oscillation in the South Asian summer monsoon region. *J. Climate*, **14 (13)**, 2910–2922, doi:10.1175/1520-0442(2001)014.

Lee, J.-Y., B. Wang, M. C. Wheeler, X. Fu, D. E. Waliser, and I.-S. Kang, 2013: Real-time multivariate indices for the boreal summer intraseasonal oscillation over the Asian summer monsoon region. *Climate Dyn.*, **40 (1-2)**, 493–509.

Liebmann, B., and A. Smith, C, 1996: Description of a Complete (Interpolated) Outgoing Longwave Radiation Dataset. *Bull. Amer. Meteor. Soc.*, **77**, 1275–1277.

Monahan, A. H., J. C. Fyfe, M. H. Ambaum, D. B. Stephenson, and G. R. North, 2009: Empirical orthogonal functions: The medium is the message. *J. Climate*, **22 (24)**, 6501–6514.

Moron, V., A. Robertson, and M. Ghil, 2012: Impact of the modulated annual cycle and intraseasonal oscillation on daily-to-interannual rainfall variability across monsoonal India. *Climate Dyn.*, **38 (11-12)**, 2409–2435, doi:10.1007/s00382-011-1253-4, URL http://dx.doi.org/10.1007/s00382-011-1253-4.

Moron, V., R. Vautard, and M. Ghil, 1998: Trends, interdecadal and interannual oscillations in global sea-surface temperatures. *Climate Dyn.*, **14 (7-8)**, 545–569, doi:10.1007/s003820050241.

Murakami, M., 1976: Analysis of summer monsoon fluctuations over India. *J. Meteor. Soc. Japan*, **54 (1)**, 15–31.

Plaut, G., and R. Vautard, 1994: Spells of low-frequency oscillations and weather regimes in the Northern Hemisphere. *J. Atmos. Sci.*, **51 (2)**, 210–236, doi:10.1175/1520-0469(1994)051.

Rajeevan, M., 2001: Prediction of Indian summer monsoon: Status, problems and prospects. *Curr. Sci.*, **81 (11)**, 1451–1458.

Rajeevan, M., S. Gadgil, and J. Bhate, 2010: Active and break spells of the Indian summer monsoon. *J. Earth. Syst. Sci.*, **119 (3)**, 229–247, doi:10.1007/s12040-010-0019-4.

Reynolds, R. W., T. M. Smith, C. Liu, D. B. Chelton, K. S. Casey, and M. G. Schlax, 2007: Daily high-resolution-blended analyses for sea surface temperature. *J. Clim.*, **20 (22)**, 5473–5496, doi:10.1175/2007JCLI1824.1.

738 Sikka, D., and S. Gadgil, 1980: On the maximum cloud zone and the ITCZ over Indian, lon-
739 gitudes during the southwest monsoon. *Mon. Wea. Rev.*, **108 (11)**, 1840–1853, doi:10.1175/
740 1520-0493(1980)108⟨1840:OTMCZA⟩2.0.CO;2.

741 Singh, S., R. Kripalani, and D. Sikka, 1992: Interannual variability of the Madden-Julian
742 oscillations in Indian summer monsoon rainfall. *J. Climate*, **5 (9)**, 973–978, doi:10.1175/
743 1520-0442(1992)005⟨0973:IVOTMJ⟩2.0.CO;2.

744 Sperber, K. R., J. M. Slingo, and H. Annamalai, 2000: Predictability and the relationship between
745 subseasonal and interannual variability during the Asian summer monsoon. *Quart. J. Roy. Me-*
746 *teor. Soc.*, **126 (568)**, 2545–2574, doi:10.1002/qj.49712656810.

747 Sperber, K. R., and Coauthors, 2001: Dynamical seasonal predictability of the Asian sum-
748 mer monsoon. *Mon. Wea. Rev.*, **129 (9)**, 2226–2248, doi:10.1175/1520-0493(2001)129⟨2226:
749 DSPOTA⟩2.0.CO;2.

750 Vautard, R., P. Yiou, and M. Ghil, 1992: Singular-spectrum analysis: A toolkit for short, noisy
751 chaotic signals. *Phys. D*, **58 (1)**, 95–126, doi:10.1016/0167-2789(92)90103-T.

752 Webster, P. J., and C. Hoyos, 2004: Prediction of monsoon rainfall and river discharge on 15-30-
753 day time scales. *Bull. Amer. Meteor. Soc.*, **85 (11)**, 1745.

754 Webster, P. J., V. O. Magaña, T. N. Palmer, J. Shukla, R. A. Tomas, M. Yanai, and T. Yasunari,
755 1998: Monsoons: Processes, predictability, and the prospects for prediction. *J. Geophys. Res.-*
756 *Oceans*, **103 (C7)**, 14 451–14 510, doi:10.1029/97JC02719.

757 Yasunari, T., 1979: Cloudiness fluctuations associated with the Northern Hemisphere summer
758 monsoon. *J. Meteor. Soc. Japan*, **57 (3)**, 227–242.

Yasunari, T., 1980: A quasi-stationary appearance of 30 to 40 day period in the cloudiness fluctuations during the summer monsoon over India. *J. Meteor. Soc. Japan*, **58**, 225–229.

Yoo, J. H., A. W. Robertson, and I.-S. Kang, 2010: Analysis of intraseasonal and interannual variability of the Asian summer monsoon using a hidden Markov model. *J. Climate*, **23 (20)**, 5498–5516.

LIST OF TABLES

TABLE 1. Correlation of LF-ISO and HF-ISO indices with seasonal rainfall anomalies over different regions.

Region	LF-ISO	HF-ISO
Central India (18°–26°N and 75°–82°E)	-0.58*	0.56*
Bay of Bengal (10°–20°N and 85°–95°E)	-0.21	0.12
Arabian Sea (10°–20°N and 60°–70°E)	-0.25	0.36
Central Equatorial Indian Ocean (5°S–5°N and 75°–85°E)	0.03	0.02

* *indicates that the correlations are significant at the 5% level.*

TABLE 2. Correlation of LF-ISO and HF-ISO indices with ISMR anomaly, ENSO, IOD and EQUINOO indices

Region	LF-ISO	HF-ISO
ISMR anomaly (normalized)	-0.64*	0.73*
ENSO index	0.42**	-0.50*
IOD index	-0.25	0.59*
EQUINOO index	-0.04	0.33

ISMR anomaly, ENSO, IOD and EQUINOO indices are defined in the text and in Figure 4

* *indicates that the correlation is significant at the 5% level.*

** *indicates that the correlation is significant at the 10% level.*

LIST OF FIGURES

2005 and **(d)** 2011 June–September. The arrow in left panel shows the eastward propagation from Arabian Sea towards India associated with LF-ISO timescale. Positive values are shaded and negative values are in dashed contours. Units are in mm/day. 46

Fig. 7. Phase composite structure of SST and positive specific humidity anomalies at 925 hPa level at different phases of LF-ISO depicted in Figure 3b. Positive SST anomalies are shaded and negative anomalies are shown as dashed contours. Stippling indicates the regions where positive specific humidity anomaly is more than 1.6×10^{-4} kg/kg. Both the anomalies are created by removing the climatology for the period 1998–2014. Then all the days are averaged which fall in each of the phases in Figure 3. Numbers in each panel indicates the phase number. Units are in K and kg/kg, respectively. Contour interval for SST is 0.04 K. . . . 47

Fig. 8. Phase-latitude diagram of LF-ISO associated rainfall and **(a)** SST, **(b)** Total column water and **(c)** Divergence anomalies along 90°E. Only LF-ISO associated positive rainfall anomaly is shown in line contours. Only positive SST, total column water and negative divergence (convergence) anomalies are shown in shaded regions. For better representation, the $x-axis$ starts from phase 6. Divergence is multiplied by a factor of and 10^6. Units of rainfall is in mm/day, SST in K, total column water in kg/m^2 and divergence in s^{-1}. 48

Fig. 9. Same as Figure 7 but for divergence anomalies at 925 hPa at different phases of LF-ISO depicted in Figure 3b. Convergence is shaded and divergence is shown in dashed contours. Unit is in s^{-1}. Contour interval for divergence is 4×10^{-7} s^{-1}. Negative in divergence implies convergence and favourable for convection. 49

Fig. 10. HF-ISO composite considering all the years (1998–2014). This is same as Figure 3b but for 10–20 days modes. Units are in mm/day. Positive values are shaded and the negative values are in thin dashed contours. The dashed and solid lines, the star and the spirals indicate different propagation characteristics. For details see the text. Stippled regions indicate regions where the values are significant in 5% significance level (using a randomization test, same as in Figure 3). 50

Fig. 11. **(a)** Time-latitude diagram of HF-ISO along 80°E during 2007 June–September. **(b)** HF-ISO composite phase-latitude diagram at 80°E. Only June-July days are taken while compositing. The arrows in **(a)** and **(b)** indicate the southward and northward movement. **(c)** Curvilinear-phase diagram for HF-ISO for June-July. For panels (b) and (c), all the years are taken into account. **(d)** Points taken to create the diagram are shown in the map, where crosses indicate the locations with points over the Indonesian coast are initial points and numbers beside the crosses indicate the respective numbers of locations. The arrow indicates the propagation along the line with phases. Positive values are shaded and negative values are in dashed contours. Units are in mm/day. 51

Fig. 12. Same as Figure 7 but for geopotential height and wind anomalies at 200 hPa level at different phases of HF-ISO depicted in Figure 10. Positive geopotential height anomalies are shaded and negative anomalies are in dashed contours. Wind is presented in vectors. Units are in m and m/s. Contour interval for geopotential height anomalies is 3 m. 52

Fig. 13. Probability of occurrence (in %) of events over central India (CI) (18°–26°N and 75°–82°E) when rainfall averaged over CI is **(a)** more than 1 standard deviation (+1-events) and **(b)** less than -1 standard deviation (−1-events) (June–September data for 17 years) in different phases of LF-ISO and HF-ISO as depicted in Figures 3b and 10. 53

Fig. 14. **(a)** LF-ISO averaged over the central India (CI) (18°–26°N and 75°–82°E) for 2003 June–October. **(b)** Raw rainfall in bars and sum of LF-ISO and HF-ISO rainfall (with added

June–October CI mean rainfall for that year) in thick line over CI for the same time period. **(c)** Same as (a), but for HF-ISO. Dotted circle in (b) indicates significant rainfall peaks as described in the text. 54

Fig. 15. LF-ISO and preferred HF-ISO phases with CI rainfall. LF-ISO phases as in Figure 3b are displayed in $x-axis$ with approximate locations of the enhanced positive rainfall anomalies associated with LF-ISO are written below the phase numbers. Dark bars indicate the rainfall amount in these LF-ISO phases. The bold numbers above the bars are the two HF-ISO phases with highest probability of occurrence in respective LF-ISO phases. The sum of the probability of occurrence of these two HF-ISO phases in respective LF-ISO phase is given in percentage values. For example, in phase 1 of LF-ISO, out of 8 HF-ISO phases 5, and 6 are the most probable phases with cumulative probability of 32%. The bars with lighter shade indicate the mean CI rainfall when the respective LF-ISO phases are accompanied by the two most probable HF-ISO phases. Unit of rainfall is in mm/day. BoB=Bay of Bengal, WG=Western Ghats, AS=Arabian Sea, CI=Central India, FH=Foothills of Himalaya, WEIO=Western equatorial Indian Ocean, CEIO=Central equatorial Indian Ocean, EEIO=Eastern equatorial Indian Ocean, PI=Peninsular India, Mrtm=Maritime continent. . . 55

Fig. 16. **(a)** In bars, normalized daily rainfall anomaly averaged over the central India (CI) (18°–26°N and 75°–82°E) for 1998 (taken as an example). The smoothed line is normalized LF-ISO rainfall averaged over CI for 1998. $y-axis$ does not have units. Dotted line indicates the angle (γ in radians) of the LF-ISO rainfall over CI calculated as discussed in text. See right $y-axis$ for ticks. Four stippled lines are -$5\pi/6$, -$\pi/6$, $\pi/6$, $5\pi/6$ radian constant lines shown to describe LF-ISO active and break episodes. If for a value of t (day), $\gamma(t) \in (\pi/6, 5\pi/6)$, LF-ISO is in active episode, and if $\gamma(t) \in (-5\pi/6, -\pi/6)$, LF-ISO is in break episode. The rest of the values of $\theta(t)$ determines the transition phase. **(b)** Similar figure for HF-ISO for 1998. **(c)** Mean percentage value of $+1$-events in active and break episodes of LF-ISO and HF-ISO as defined described in a Venn-diagram, considering all the years. **(d)** Similar figure for -1-events. L^+ and L^- indicates the LF-ISO active and break episodes. H^+ and H^- indicates the same for HF-ISO. Numbers written in % indicate the amount of +1 (-1) events occurred in the given episode. % values in bold and italics gives the amount of events occurred in the intersection of two given episodes. % values outside the circles indicate the amount that occurred in transition phases and are not considered here. All the % values are significant at the 5% level (using a randomization test). 56

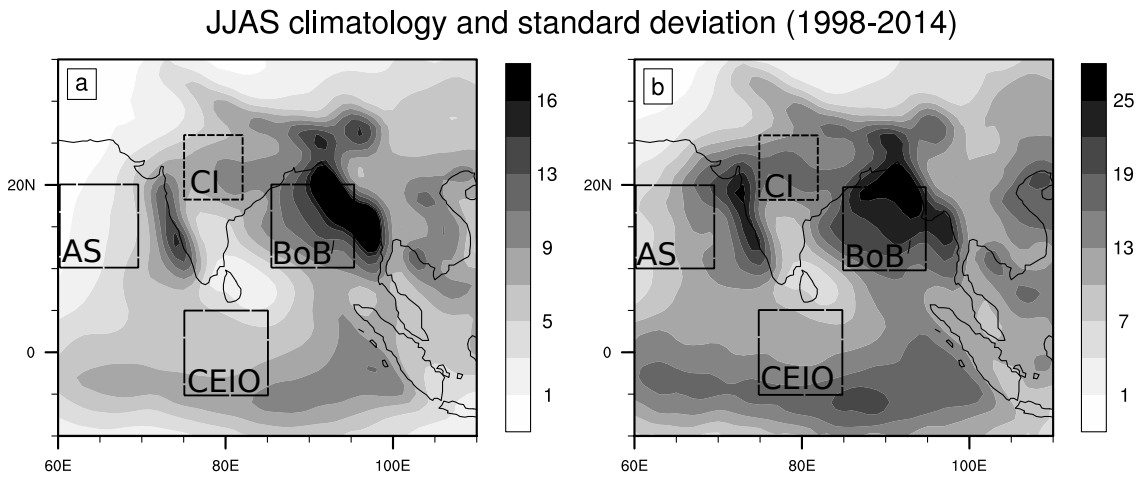

FIG. 1. **(a)** Daily climatology and **(b)** Daily standard deviation of TRMM 3B42v2 rainfall for the period 1998–2014. Units are in mm/day. Boxes indicate the central Indian (CI) region, Arabian Sea (AS), Bay of Bengal (BoB) and central equatorial Indian Ocean (CEIO) region used in the analysis later on.

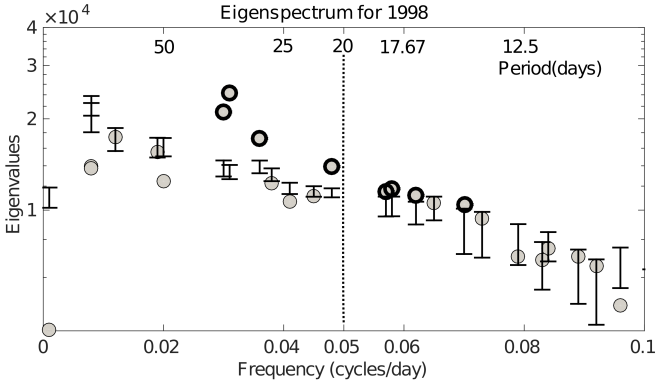

FIG. 2. Eigenvalues from MSSA for 1998 May–October rainfall over the given region against the dominant frequency associated with their corresponding eigenvectors from MSSA given with statistical significance level (zoomed into the region of interest). Error bars represent the 2.5% and 97.5% quantile from an ensemble of 1000 surrogate data. Eigenmodes which lie above the corresponding errorbars are considered as significant. The significant eigenmodes are plotted in thick circles and modes that are not significant are shown in thin circles. For example, eigenmodes 1 and 2 with periodicities almost 33 days are considered as significant. Significant modes with time-periods within 20–60 days and 10–20 days are considered as LF-ISO and HF-ISO modes, respectively. The dotted vertical line separates LF-ISO and HF-ISO modes.

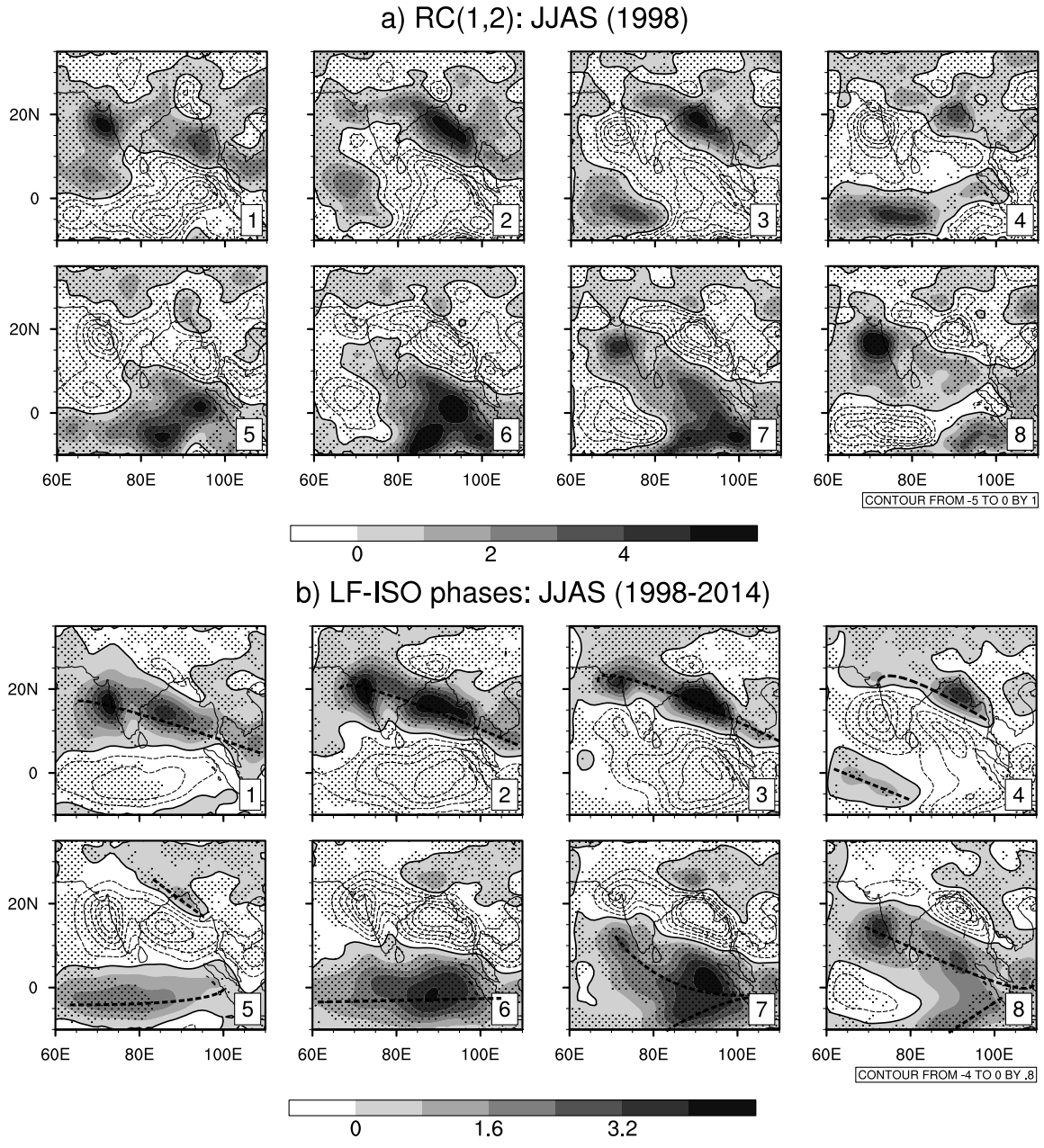

FIG. 3. **(a)** Reconstructed components 1 and 2 ($RC(1,2)$) for 1998 in eight phases with phases are defined as in text. **(b)** LF-ISO composite for all the years (1998–2014). All the significant modes each year having periodicity within 20–60 days range are used to create this composite. For both the panels, days during June-September only are used for compositing. Numbers in each panel indicates the phase numbers. Positive values are shaded and negative values are given by thin dotted contours. In panel (b) rainfall belts are thick dotted lines. Units are in mm/day. The dotted lines in each phase show the dominant rainfall belt associated with LF-ISO in that phase. Stippled regions indicate regions where the values are significant in 5% significance level (Significance is tested by randomly permuting the 8-phases (all possible permutations are used) and comparing the anomalies obtained from the re-shuffled phases with the observed ones).

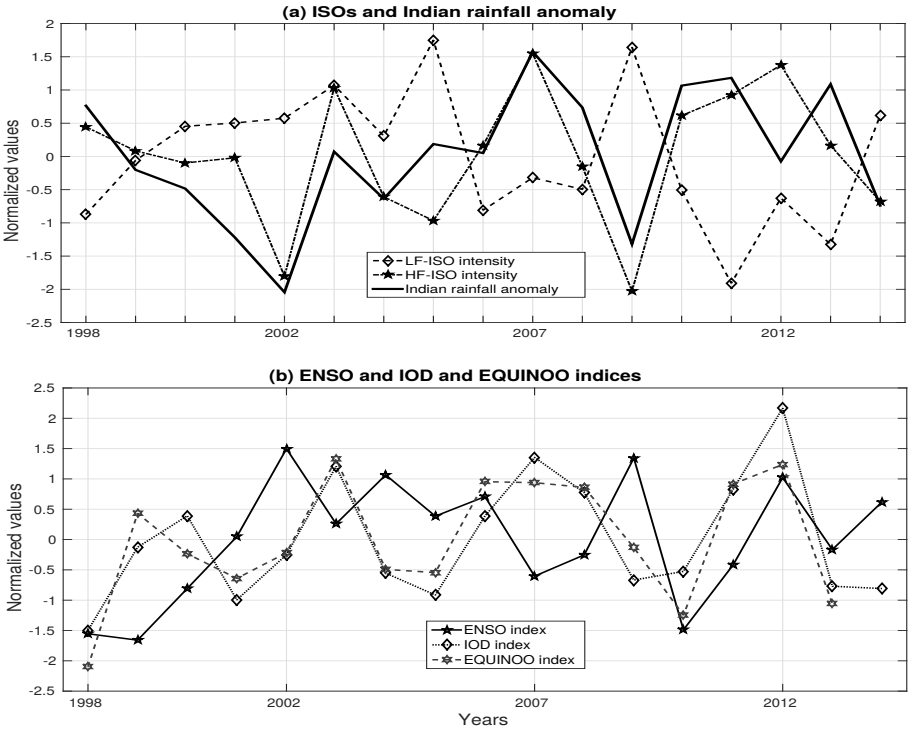

FIG. 4. **(a)** LF-ISO and HF-ISO indices and all-India summer monsoon rainfall (ISMR) anomaly (calculated over Indian land except the north and northeastern hilly regions). Anomaly is based on removing the 17-years climatology. All the fields are normalized by their own standard deviations. **(b)** Normalized June–September mean SST anomaly over Niño-3.4 region (5°S–5°N and 190°–240°E) (ENSO index), normalized difference between June–September mean SST anomalies over western and eastern equatorial Indian Ocean (WEIO (10°S–10°N and 50°–70°E) and EEIO (10°S–0° and 90°–110°E)) (IOD index), and normalized difference between June–September mean OLR anomalies over EEIO and WEIO (EQUINOO index). These indices are calculated based on only 17 (16 for EQUINOO) years data. OLR data is given upto 2013.

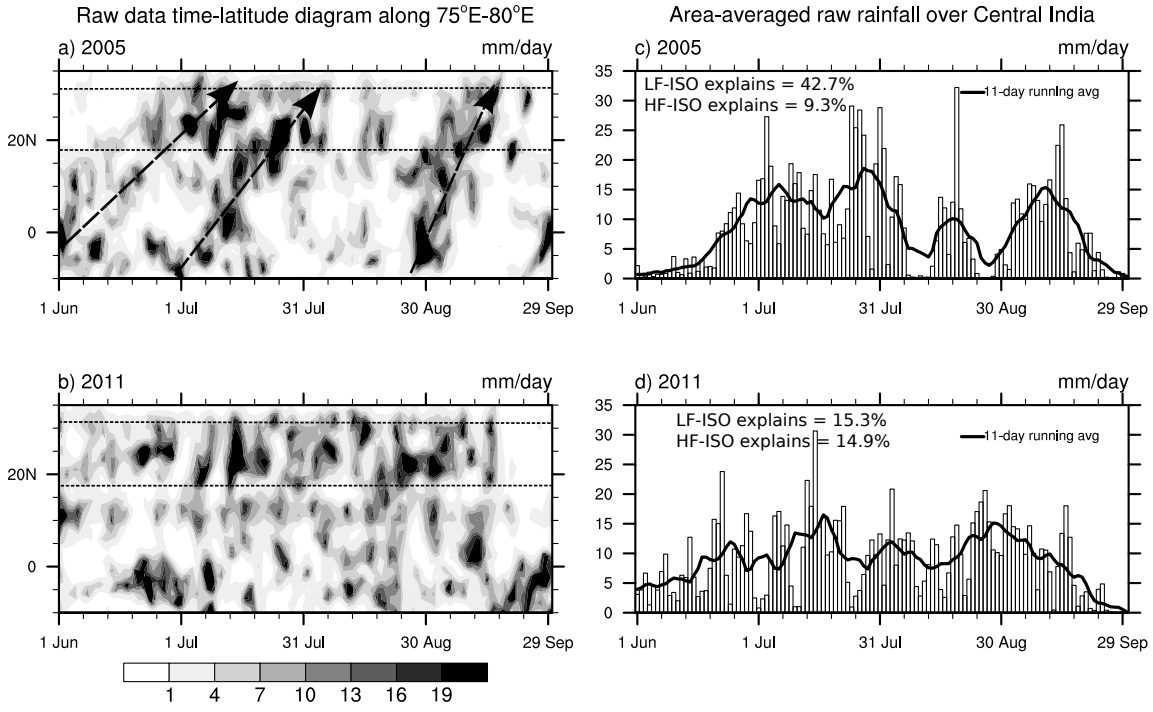

FIG. 5. **(a)** Time-latitude diagram of rainfall averaged between 75°E-80°E during 2005 June–September. **(b)** Same as (a), but for 2011. **(c)** Time series of daily rainfall over central Indian region (18°N to 26°N, 75°E to 82°E) for 2005 June–September. Arrows in panels (a) and (c) show the northward propagation of rainfall from the equatorial region. Horizontal dotted lines in panels (a) and (b) show the latitudes of the CI box. Solid line indicates 11-day running average. **(d)** Same as (c), but for 2011. In panels (c) and (d), the percentage values indicate the contribution of each ISO mode towards the total variability (5-day smoothed) for the given year over the entire region.

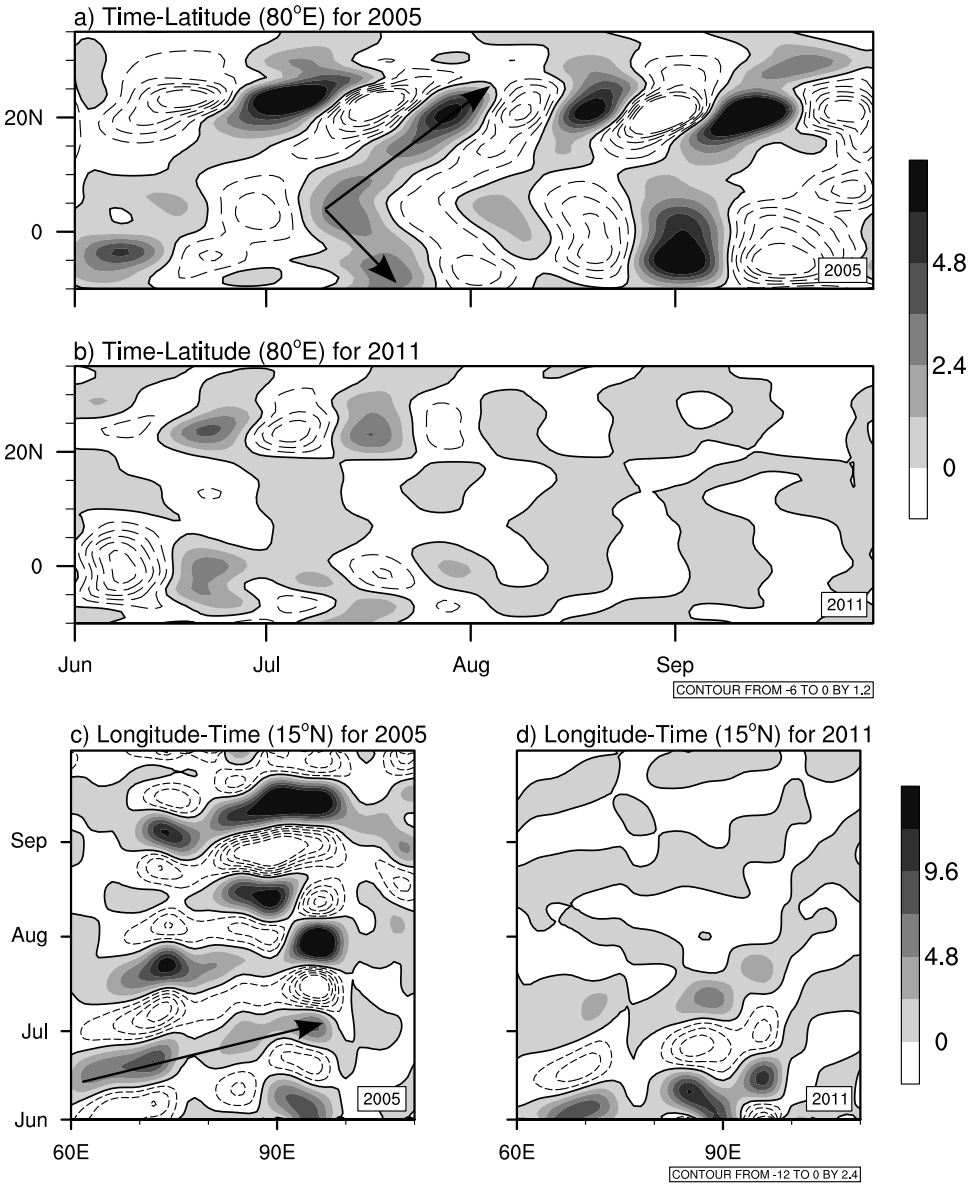

928 FIG. 6. Time-latitude diagram of LF-ISO along 80°E during **(a)** 2005 and **(b)** 2011 June–September. The
929 arrows in upper panel show the northward and southward propagation from the equator associated with LF-ISO
930 scale. Longitude-time diagram of LF-ISO along 15°N during **(c)** 2005 and **(d)** 2011 June–September. The arrow
931 in left panel shows the eastward propagation from Arabian Sea towards India associated with LF-ISO timescale.
932 Positive values are shaded and negative values are in dashed contours. Units are in mm/day.

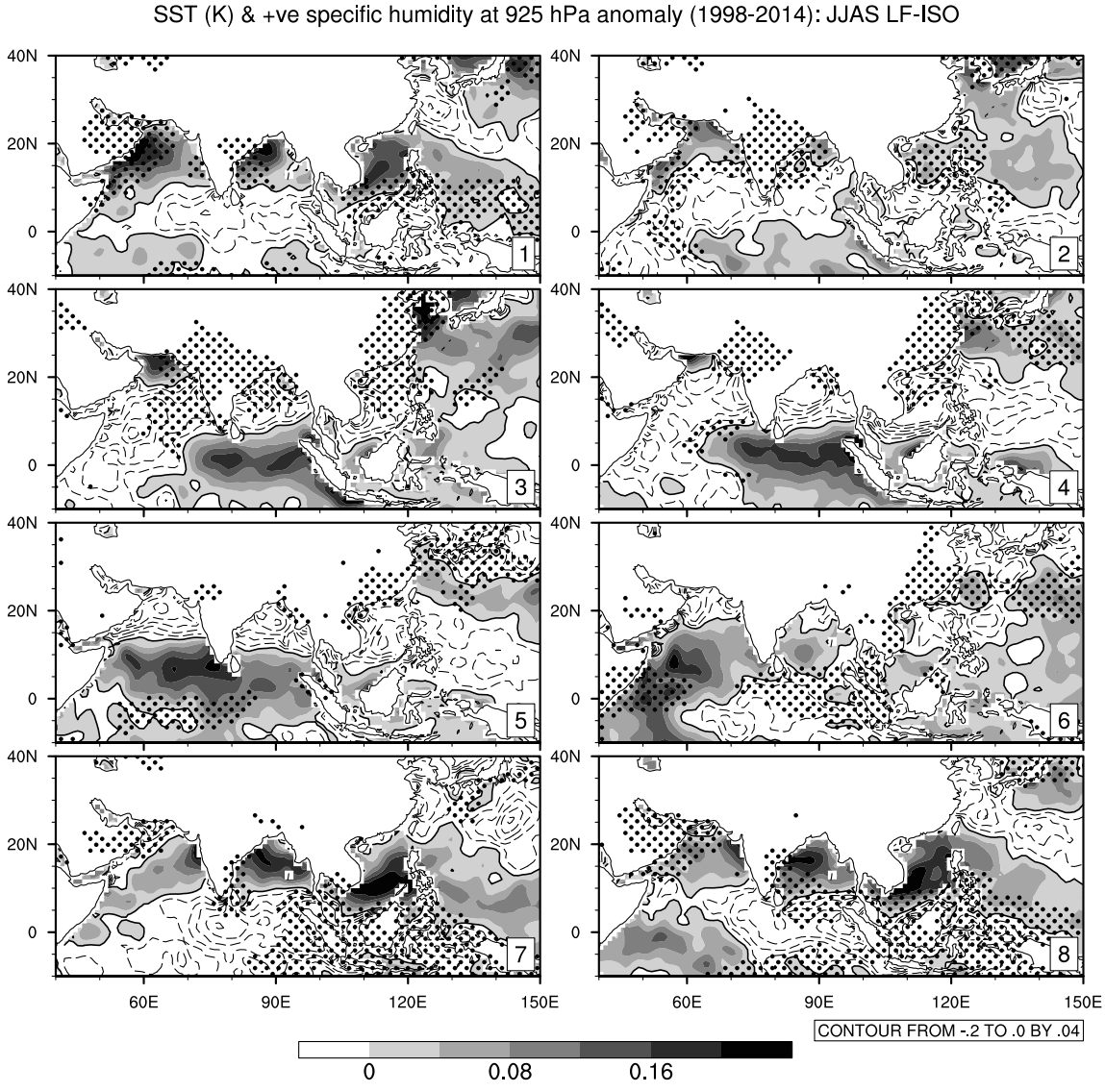

933 FIG. 7. Phase composite structure of SST and positive specific humidity anomalies at 925 hPa level at different
934 phases of LF-ISO depicted in Figure 3b. Positive SST anomalies are shaded and negative anomalies are shown
935 as dashed contours. Stippling indicates the regions where positive specific humidity anomaly is more than 1.6
936 $\times 10^{-4}\ kg/kg$. Both the anomalies are created by removing the climatology for the period 1998–2014. Then all
937 the days are averaged which fall in each of the phases in Figure 3. Numbers in each panel indicates the phase
938 number. Units are in K and kg/kg, respectively. Contour interval for SST is 0.04 K.

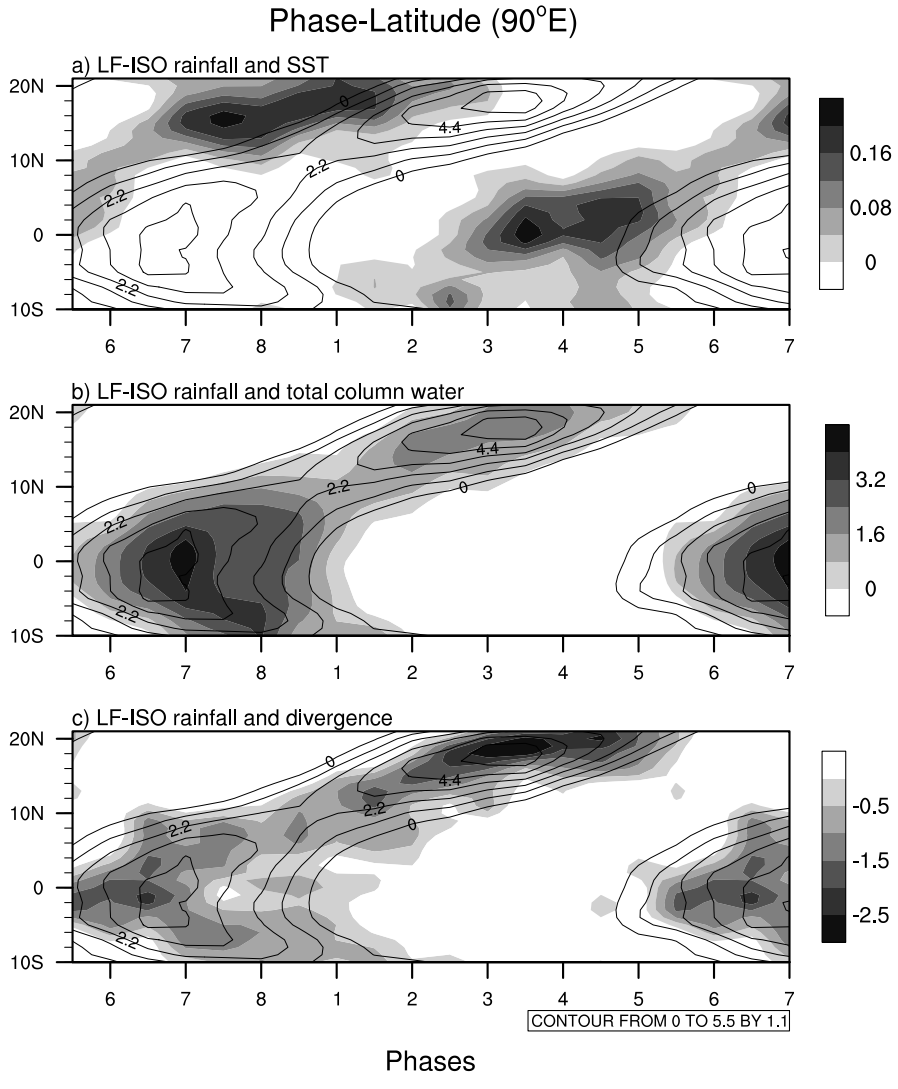

939 FIG. 8. Phase-latitude diagram of LF-ISO associated rainfall and **(a)** SST, **(b)** Total column water and **(c)**
940 Divergence anomalies along 90°E. Only LF-ISO associated positive rainfall anomaly is shown in line contours.
941 Only positive SST, total column water and negative divergence (convergence) anomalies are shown in shaded
942 regions. For better representation, the $x-axis$ starts from phase 6. Divergence is multiplied by a factor of and
943 10^6. Units of rainfall is in mm/day, SST in K, total column water in kg/m^2 and divergence in s^{-1}.

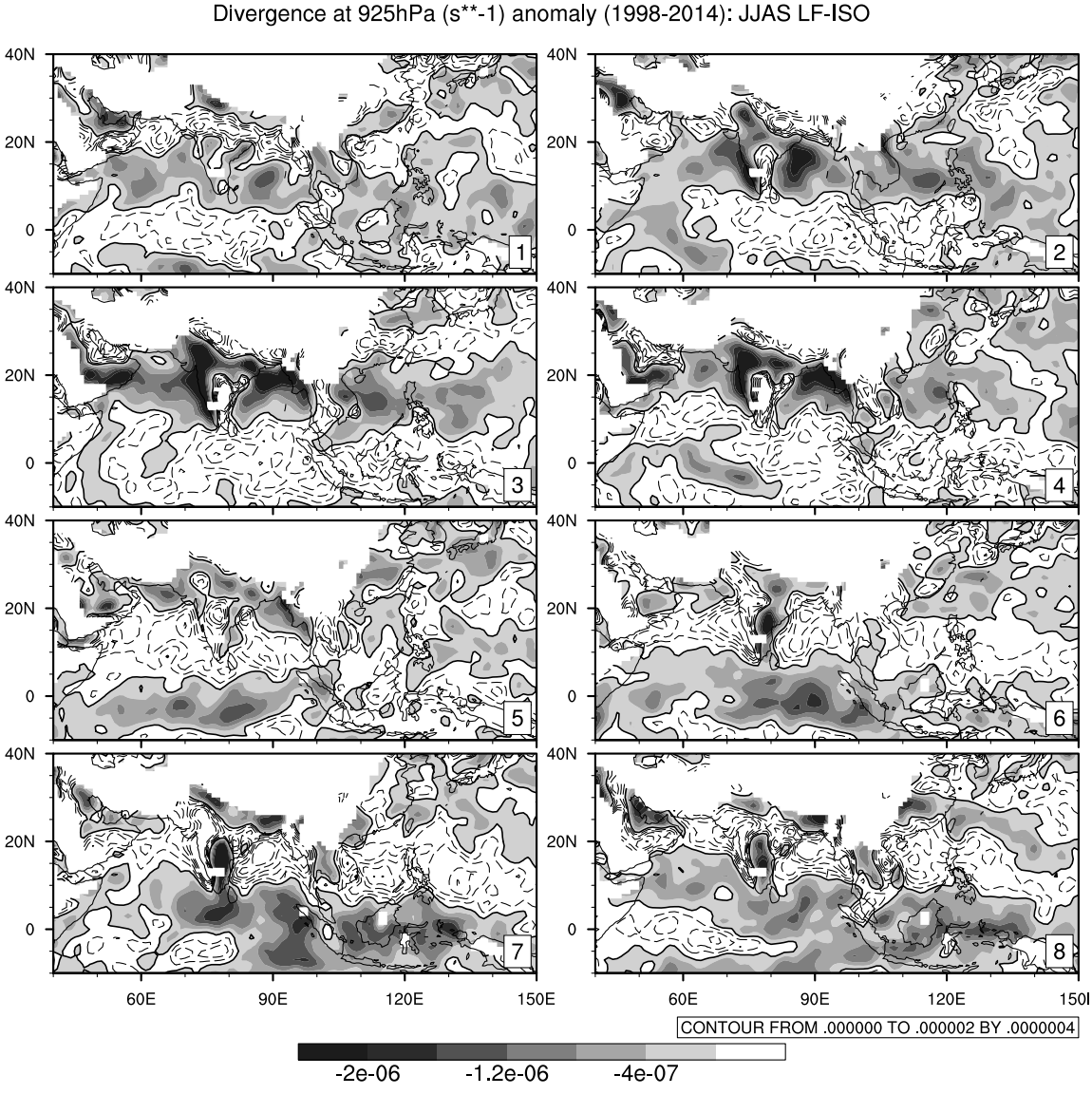

944 FIG. 9. Same as Figure 7 but for divergence anomalies at 925 hPa at different phases of LF-ISO depicted in
945 Figure 3b. Convergence is shaded and divergence is shown in dashed contours. Unit is in s^{-1}. Contour interval
946 for divergence is $4 \times 10^{-7}\ s^{-1}$. Negative in divergence implies convergence and favourable for convection.

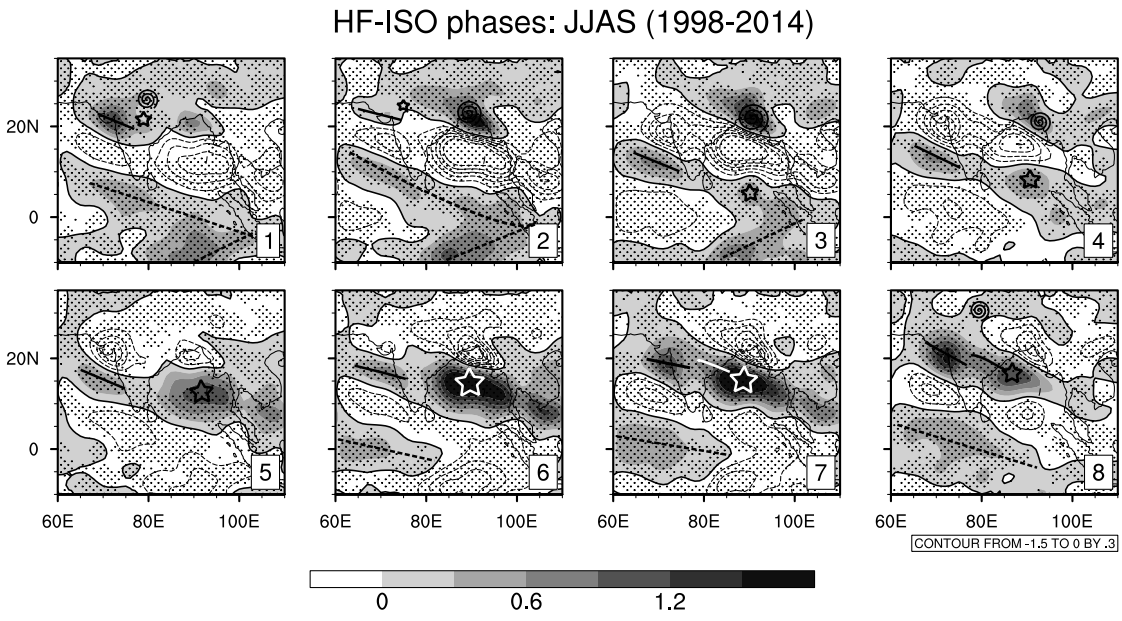

947 FIG. 10. HF-ISO composite considering all the years (1998–2014). This is same as Figure 3b but for 10–
948 20 days modes. Units are in mm/day. Positive values are shaded and the negative values are in thin dashed
949 contours. The dashed and solid lines, the star and the spirals indicate different propagation characteristics. For
950 details see the text. Stippled regions indicate regions where the values are significant in 5% significance level
951 (using a randomization test, same as in Figure 3).

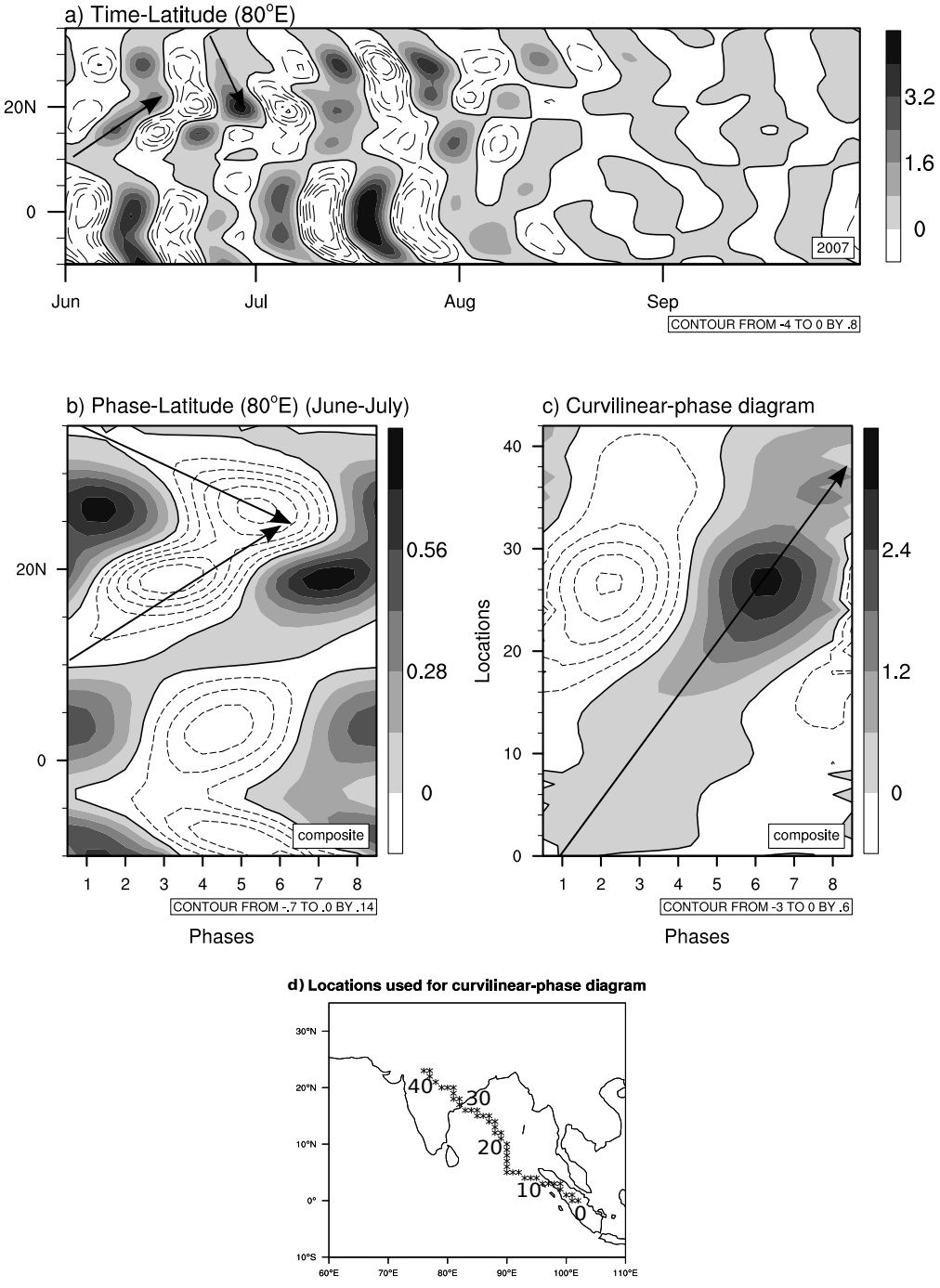

FIG. 11. **(a)** Time-latitude diagram of HF-ISO along 80°E during 2007 June–September. **(b)** HF-ISO composite phase-latitude diagram at 80°E. Only June-July days are taken while compositing. The arrows in **(a)** and **(b)** indicate the southward and northward movement. **(c)** Curvilinear-phase diagram for HF-ISO for June-July. For panels (b) and (c), all the years are taken into account. **(d)** Points taken to create the diagram are shown in the map, where crosses indicate the locations with points over the Indonesian coast are initial points and numbers beside the crosses indicate the respective numbers of locations. The arrow indicates the propagation along the line with phases. Positive values are shaded and negative values are in dashed contours. Units are in mm/day.

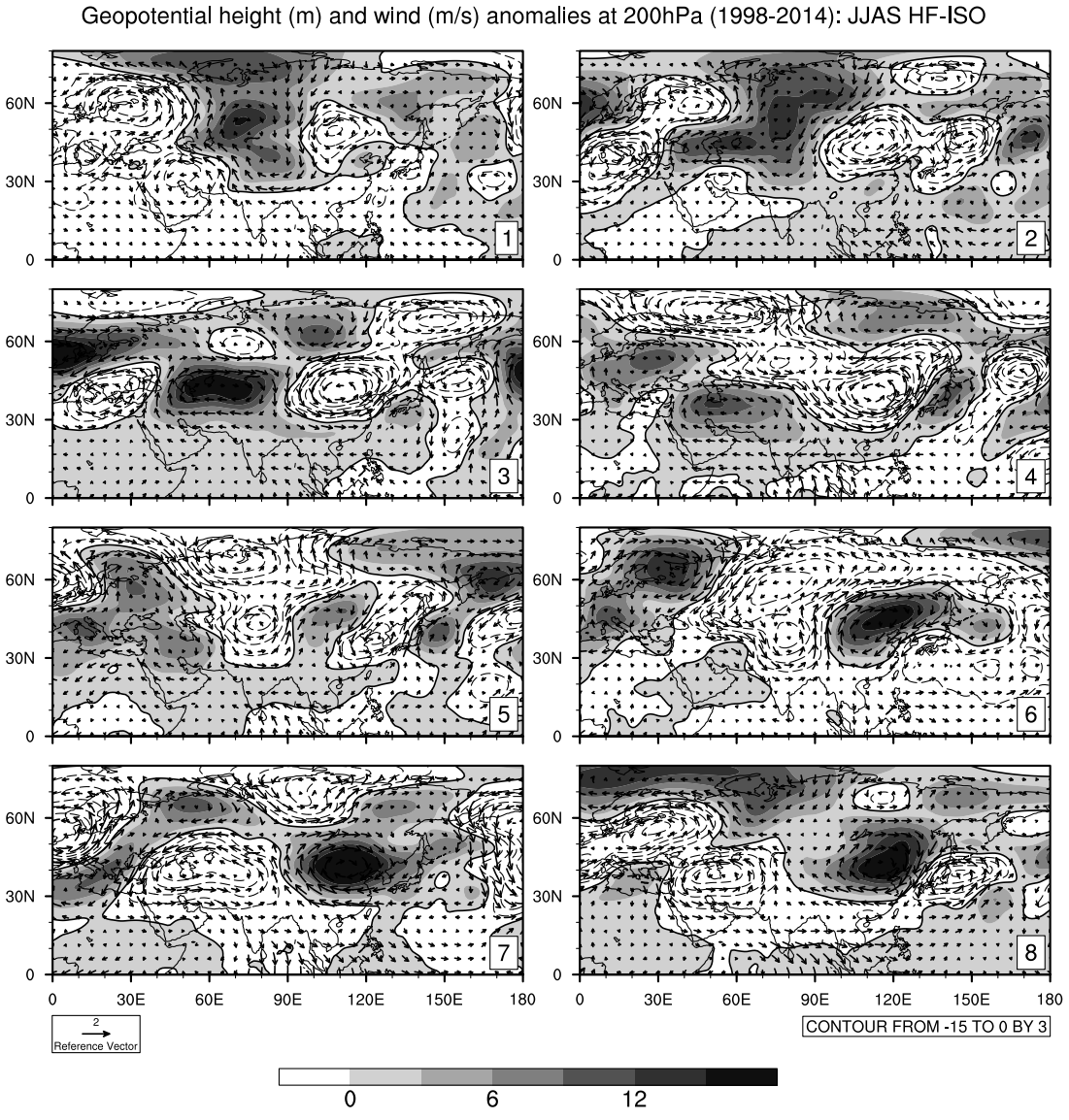

959 FIG. 12. Same as Figure 7 but for geopotential height and wind anomalies at 200 hPa level at different phases
960 of HF-ISO depicted in Figure 10. Positive geopotential height anomalies are shaded and negative anomalies are
961 in dashed contours. Wind is presented in vectors. Units are in m and m/s. Contour interval for geopotential
962 height anomalies is 3 m.

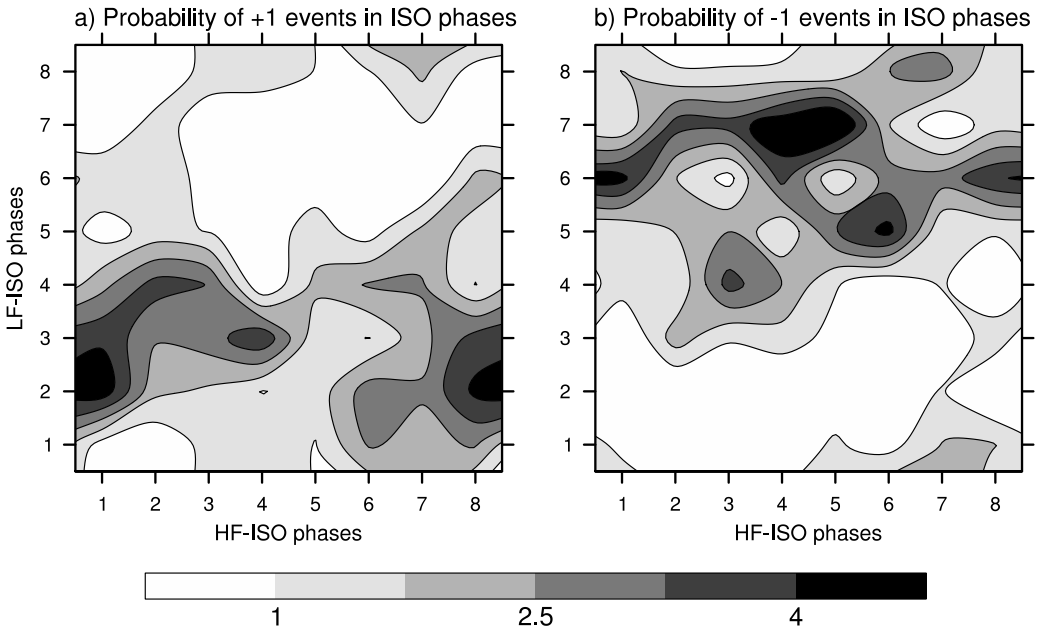

963 FIG. 13. Probability of occurrence (in %) of events over central India (CI) (18°–26°N and 75°–82°E) when
964 rainfall averaged over CI is **(a)** more than 1 standard deviation (+1-events) and **(b)** less than -1 standard deviation
965 (−1-events) (June–September data for 17 years) in different phases of LF-ISO and HF-ISO as depicted in Figures
966 3b and 10.

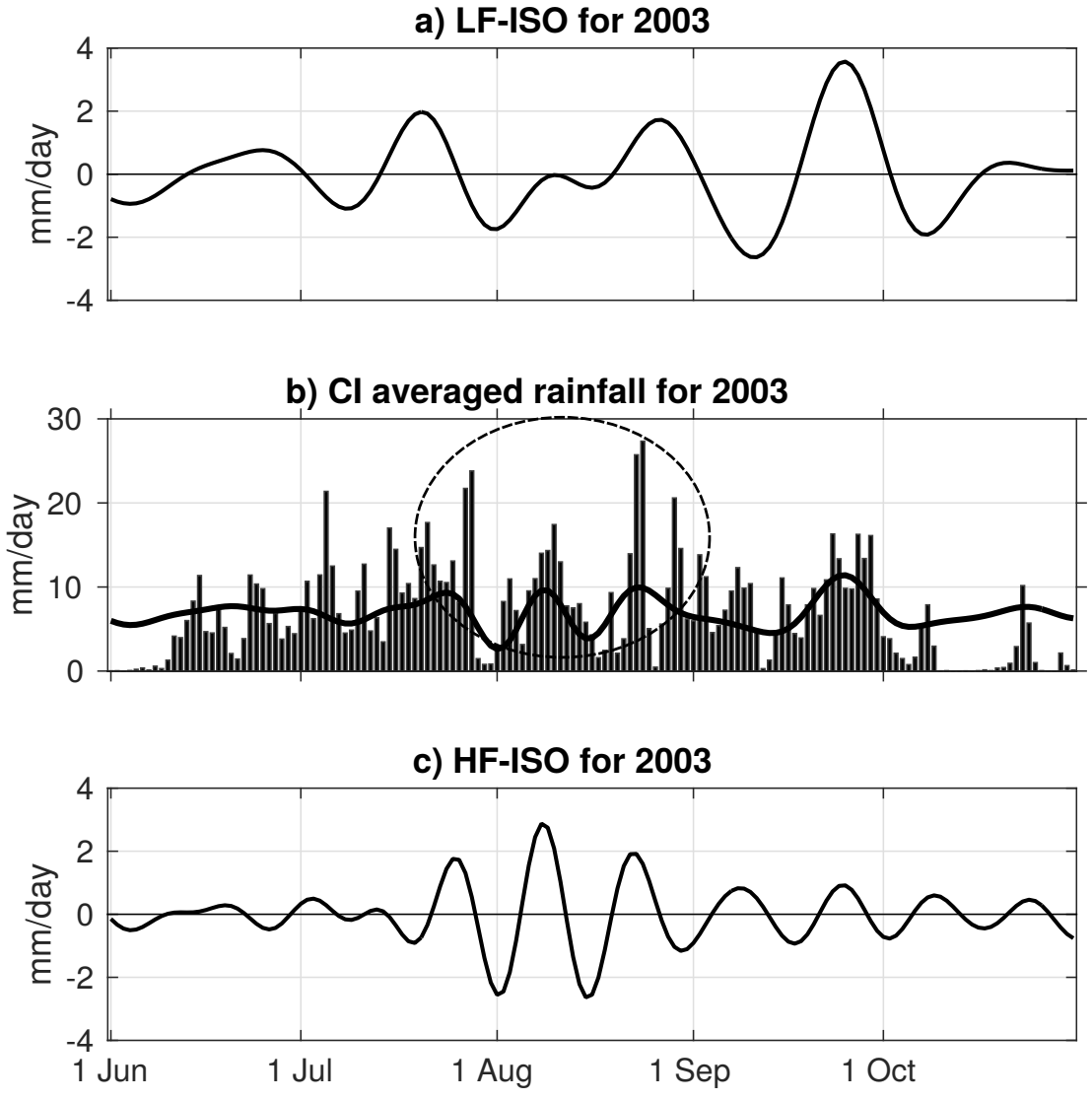

FIG. 14. **(a)** LF-ISO averaged over the central India (CI) (18°–26°N and 75°–82°E) for 2003 June–October. **(b)** Raw rainfall in bars and sum of LF-ISO and HF-ISO rainfall (with added June–October CI mean rainfall for that year) in thick line over CI for the same time period. **(c)** Same as (a), but for HF-ISO. Dotted circle in (b) indicates significant rainfall peaks as described in the text.

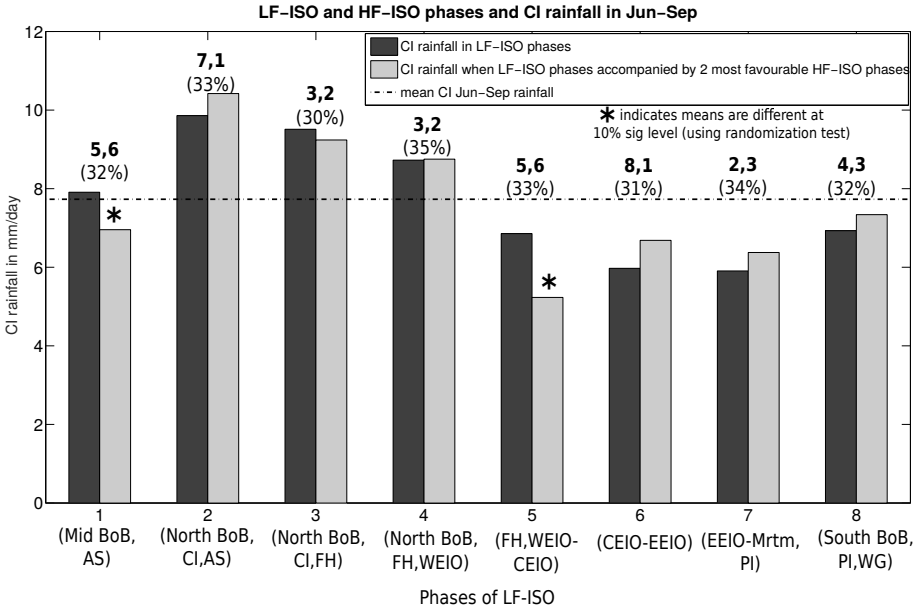

FIG. 15. LF-ISO and preferred HF-ISO phases with CI rainfall. LF-ISO phases as in Figure 3b are displayed in $x-axis$ with approximate locations of the enhanced positive rainfall anomalies associated with LF-ISO are written below the phase numbers. Dark bars indicate the rainfall amount in these LF-ISO phases. The bold numbers above the bars are the two HF-ISO phases with highest probability of occurrence in respective LF-ISO phases. The sum of the probability of occurrence of these two HF-ISO phases in respective LF-ISO phase is given in percentage values. For example, in phase 1 of LF-ISO, out of 8 HF-ISO phases 5, and 6 are the most probable phases with cumulative probability of 32%. The bars with lighter shade indicate the mean CI rainfall when the respective LF-ISO phases are accompanied by the two most probable HF-ISO phases. Unit of rainfall is in mm/day. BoB=Bay of Bengal, WG=Western Ghats, AS=Arabian Sea, CI=Central India, FH=Foothills of Himalaya, WEIO=Western equatorial Indian Ocean, CEIO=Central equatorial Indian Ocean, EEIO=Eastern equatorial Indian Ocean, PI=Peninsular India, Mrtm=Maritime continent.

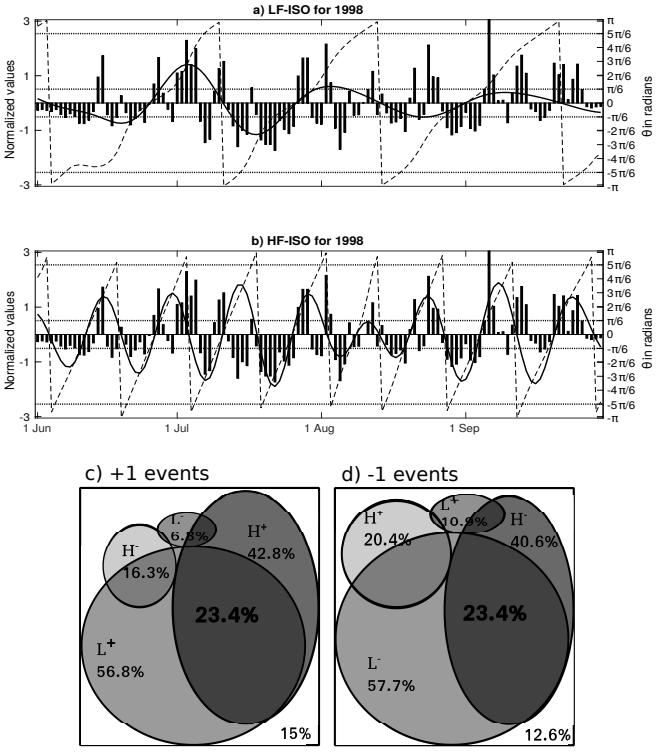

FIG. 16. **(a)** In bars, normalized daily rainfall anomaly averaged over the central India (CI) (18°–26°N and 75°–82°E) for 1998 (taken as an example). The smoothed line is normalized LF-ISO rainfall averaged over CI for 1998. $y-axis$ does not have units. Dotted line indicates the angle (γ in radians) of the LF-ISO rainfall over CI calculated as discussed in text. See right $y-axis$ for ticks. Four stippled lines are -$5\pi/6$, -$\pi/6$, $\pi/6$, $5\pi/6$ radian constant lines shown to describe LF-ISO active and break episodes. If for a value of t (day), $\gamma(t) \in (\pi/6, 5\pi/6)$, LF-ISO is in active episode, and if $\gamma(t) \in (-5\pi/6, -\pi/6)$, LF-ISO is in break episode. The rest of the values of $\theta(t)$ determines the transition phase. **(b)** Similar figure for HF-ISO for 1998. **(c)** Mean percentage value of $+1$-events in active and break episodes of LF-ISO and HF-ISO as defined described in a Venn-diagram, considering all the years. **(d)** Similar figure for -1-events. L^+ and L^- indicates the LF-ISO active and break episodes. H^+ and H^- indicates the same for HF-ISO. Numbers written in % indicate the amount of +1 (-1) events occurred in the given episode. % values in bold and italics gives the amount of events occurred in the intersection of two given episodes. % values outside the circles indicate the amount that occurred in transition phases and are not considered here. All the % values are significant at the 5% level (using a randomization test).